# Tetranuclear Iron Clusters with A Varied Interstitial Ligand: Effects On Structure, Redox Properties, and Nitric Oxide Activation

Christopher J. Reed, and Theodor Agapie*

*Division of Chemistry and Chemical Engineering, California Institute of Technology,*

*Pasadena, California 91125, United States, Email: agapie@caltech.edu*

## Supporting Information

## Table of Contents

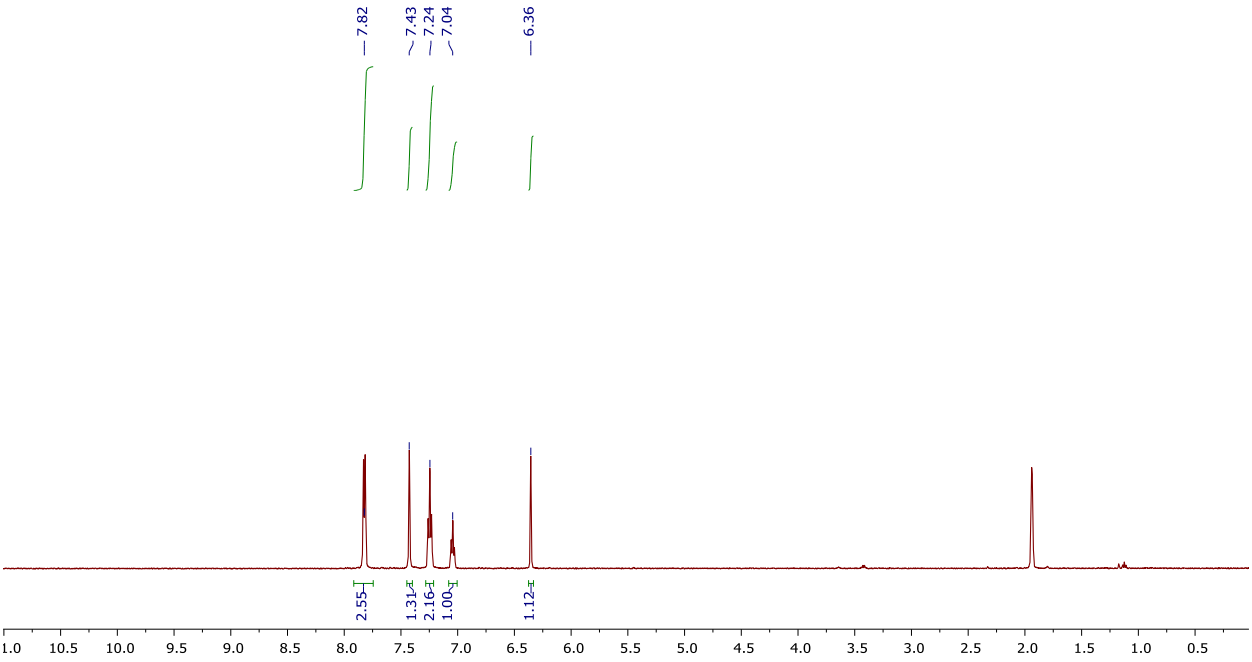


**Figure S1**. $^{1}H$ NMR spectrum (300 MHz) of potassium 3-phenyl pyrazolate in $CD_3CN$

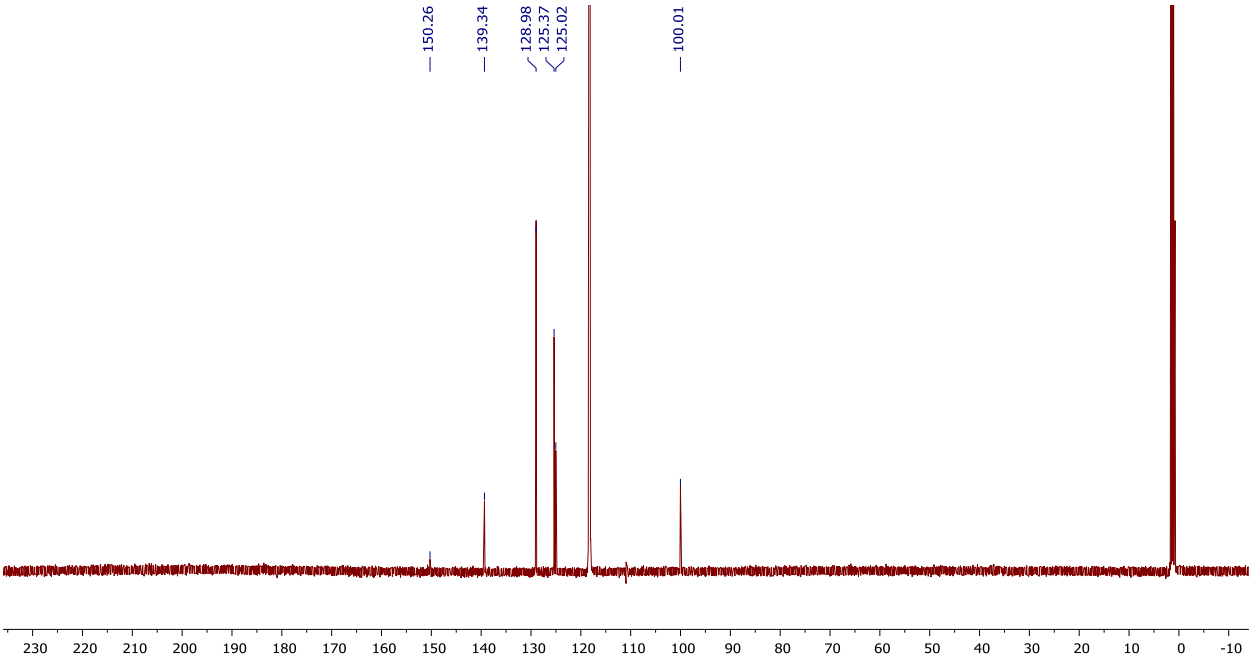


**Figure S2**. $^{13}C$ NMR spectrum (300 MHz) of potassium 3-phenyl pyrazolate in $CD_3CN$

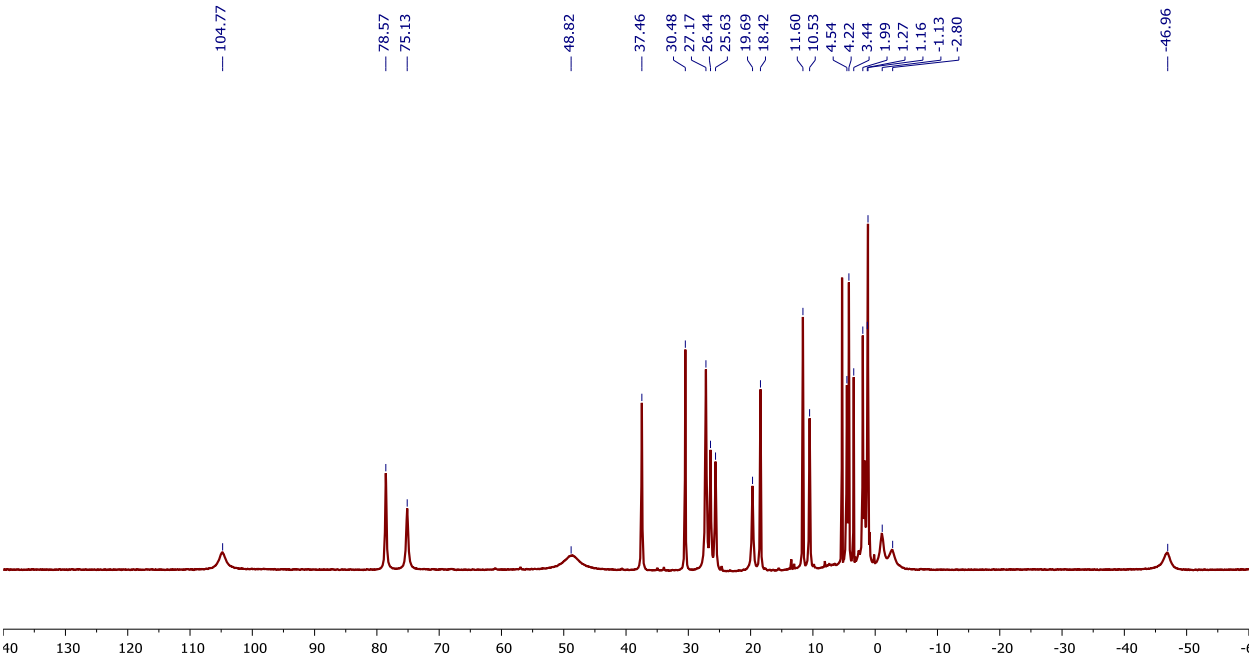


**Figure S3**. $^{1}$H NMR spectrum (300 MHz) of [$LFe_3F(PhPz)_3Fe$][OTf] (**1**) in $CD_2Cl_2$

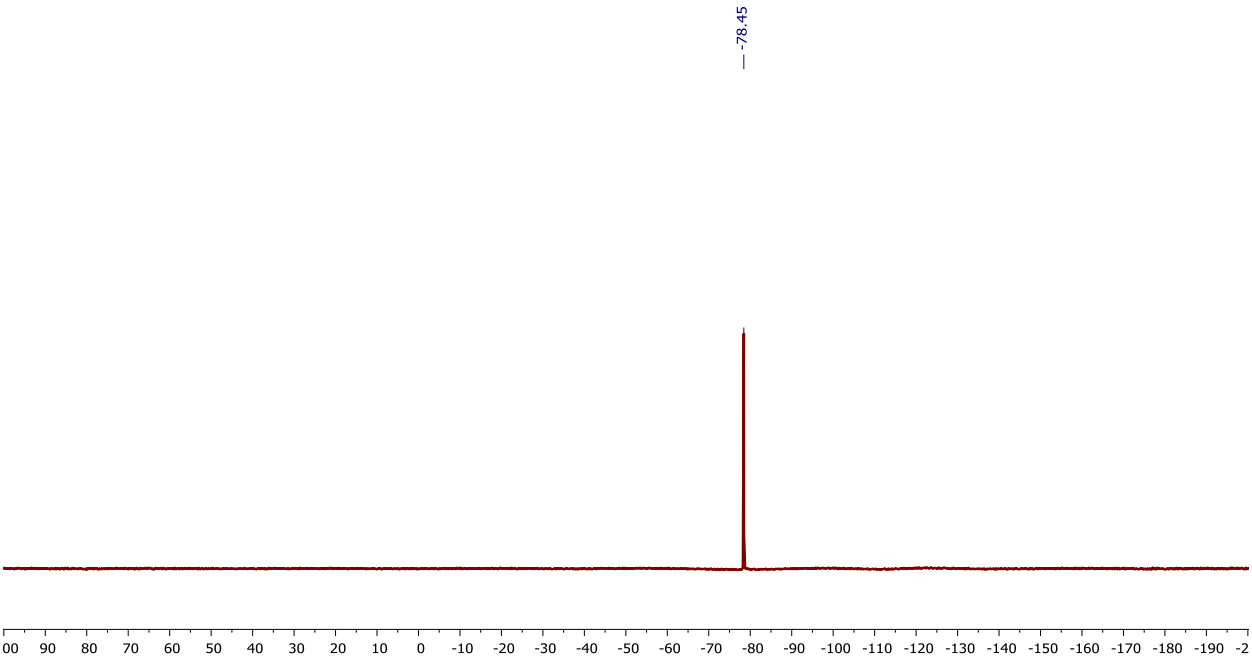


**Figure S4**. $^{19}$F NMR spectrum (300 MHz) of [$LFe_3F(PhPz)_3Fe$][OTf] (**1**) in $CD_2Cl_2$

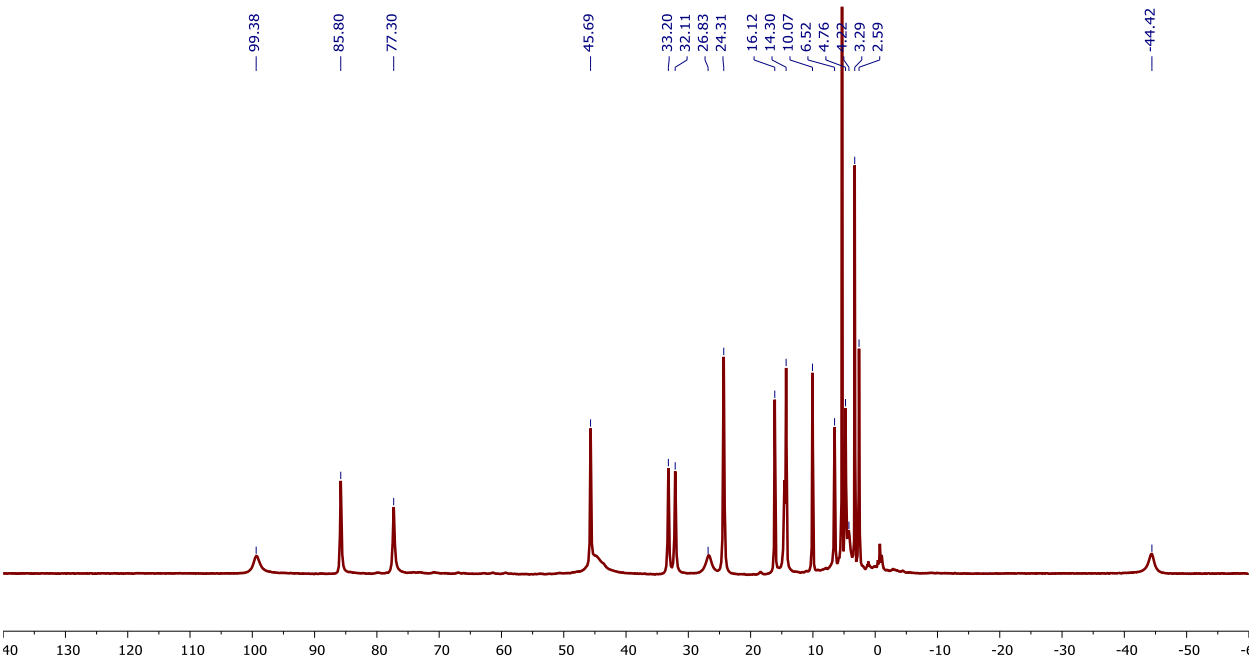


**Figure S5**. $^{1}$H NMR spectrum (300 MHz) of $[LFe_3F(PhPz)_3Fe][OTf]_2$ (**2**) in $CD_2Cl_2$

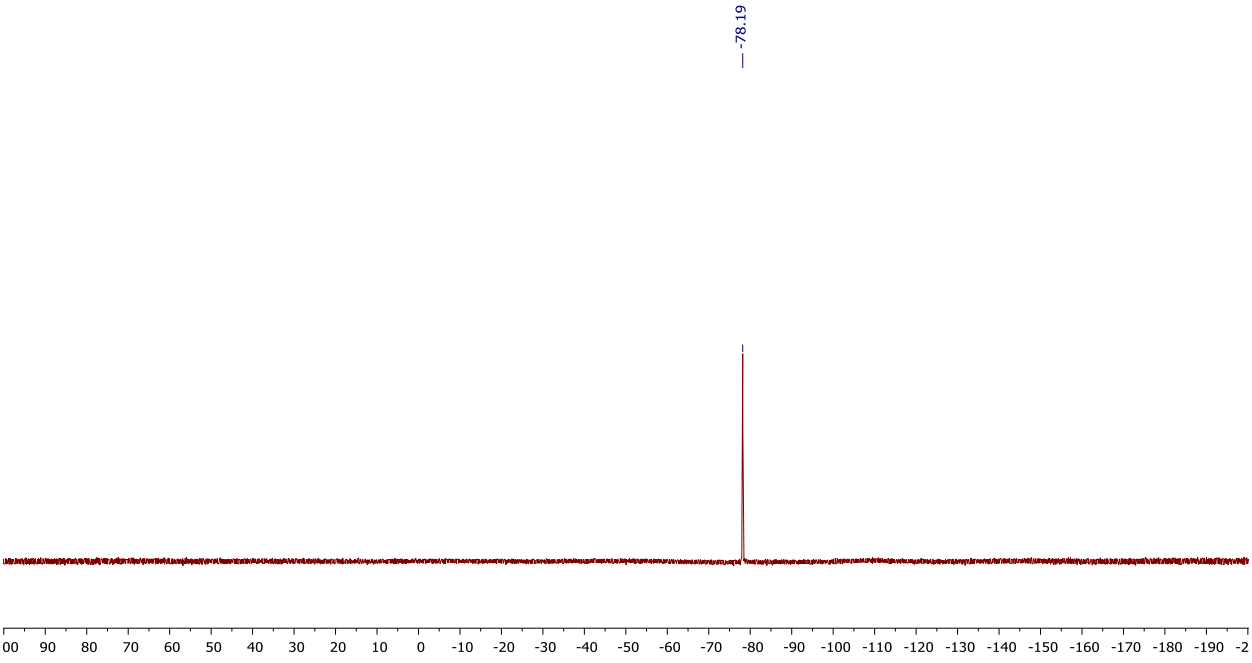


**Figure S6**. $^{19}$F NMR spectrum (300 MHz) of $[LFe_3F(PhPz)_3Fe][OTf]_2$ (**2**) in $CD_2Cl_2$

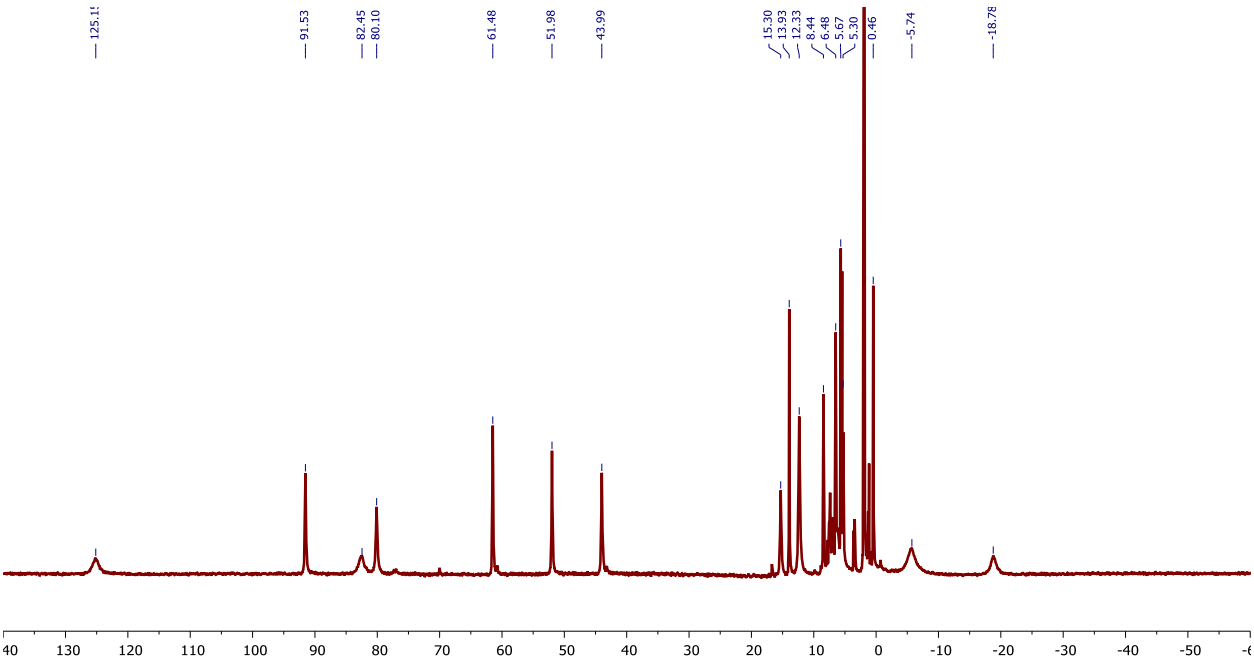


**Figure S7**. $^{1}$H NMR spectrum (300 MHz) of $[LFe_3F(PhPz)_3Fe(CH_3CN)][OTf]_3$ (**3**) in $CD_3CN$

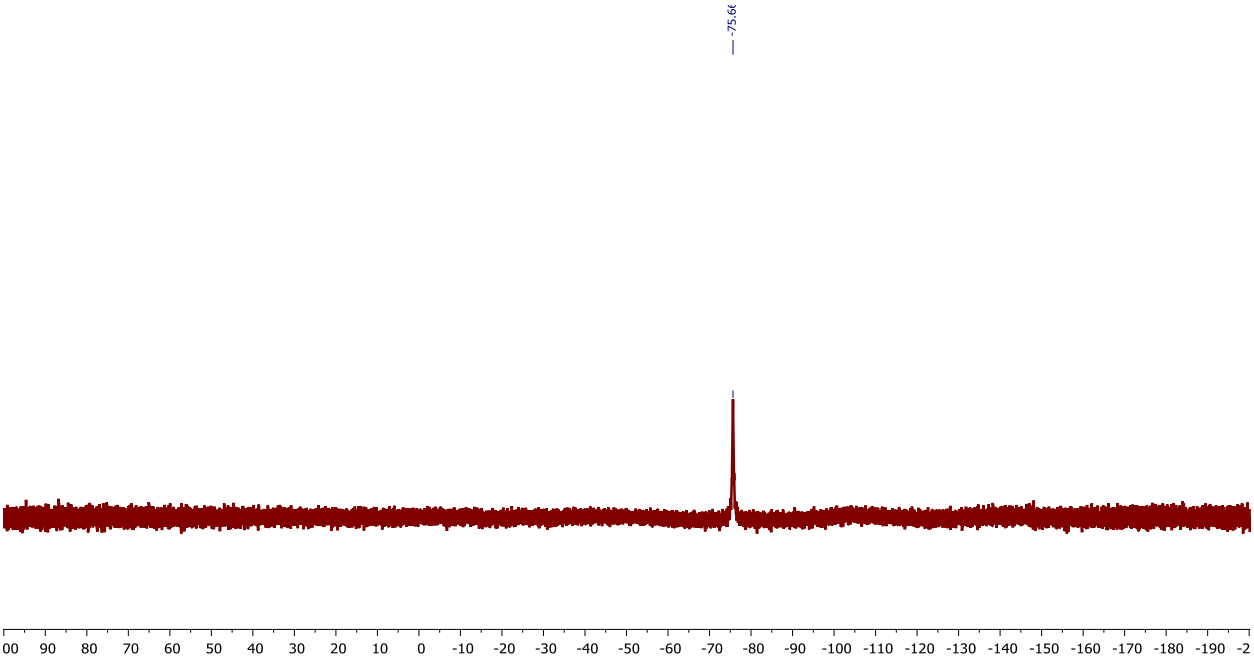


**Figure S8**. $^{19}$F NMR spectrum (300 MHz) of $[LFe_3F(PhPz)_3Fe(CH_3CN)][OTf]_3$ (**3**) in $CD_3CN$

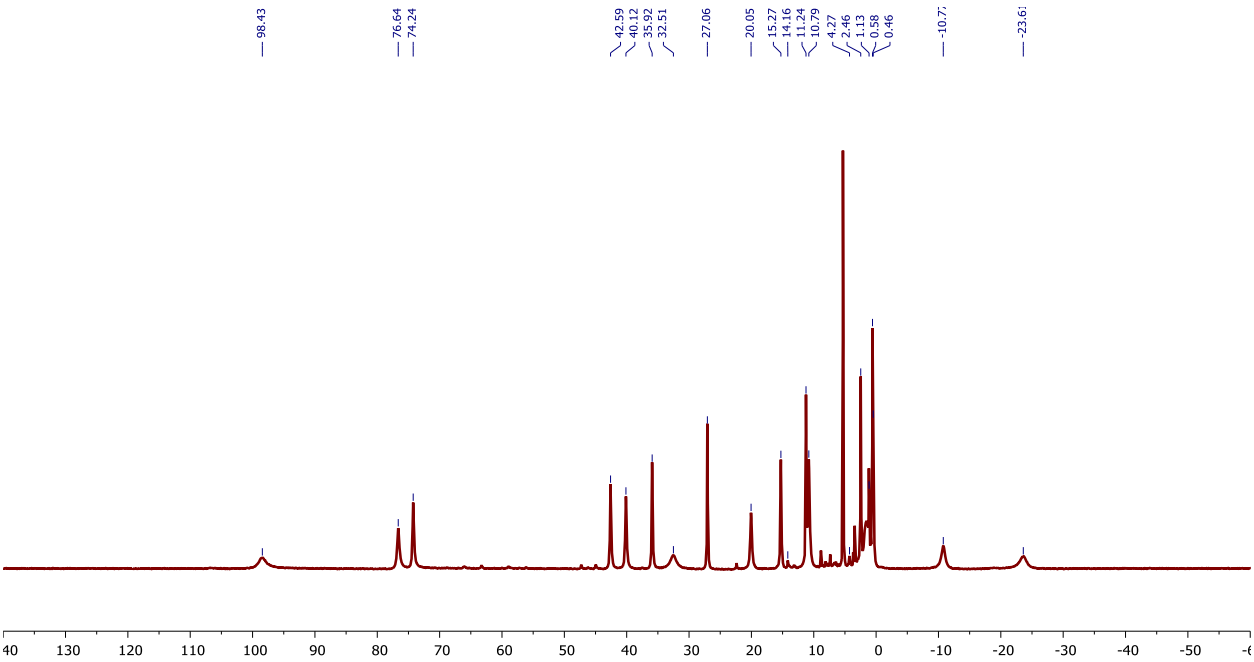


**Figure S9**. $^{1}$H NMR spectrum (300 MHz) of [$LFe_3F(PhPz)_3Fe(NO)$][OTf] (**1-NO**) in $CD_2Cl_2$

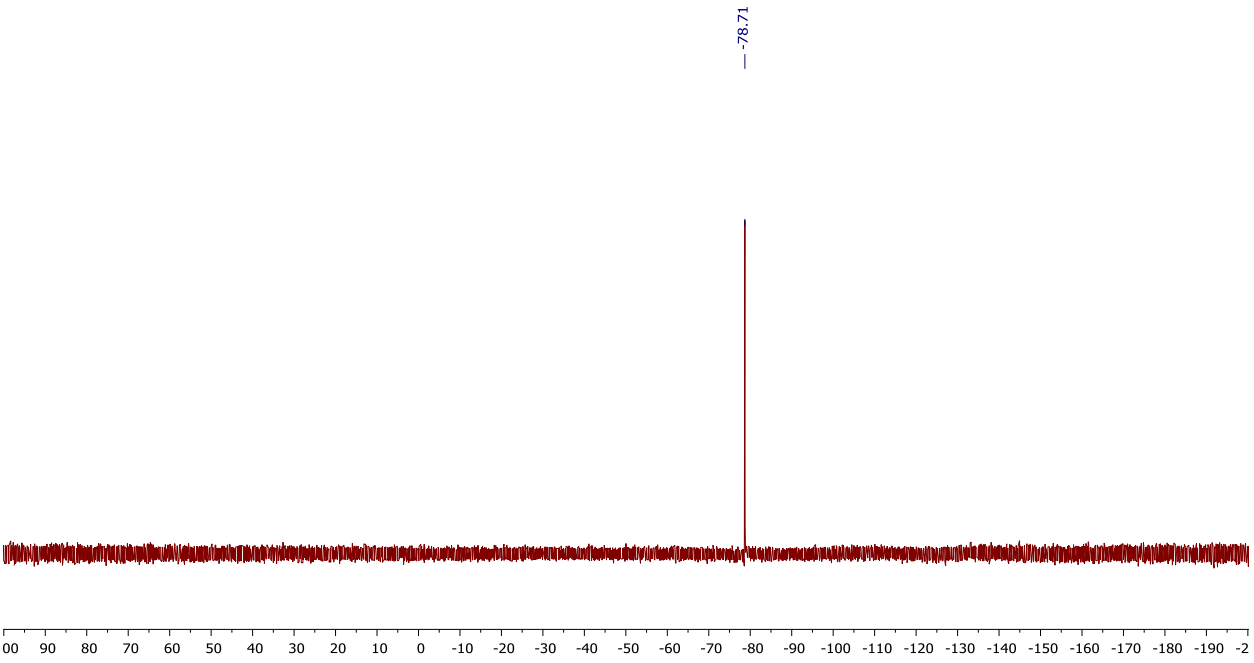


**Figure S10**. $^{19}$F NMR spectrum (300 MHz) of [$LFe_3F(PhPz)_3Fe(NO)$][OTf] (**1-NO**) in $CD_2Cl_2$

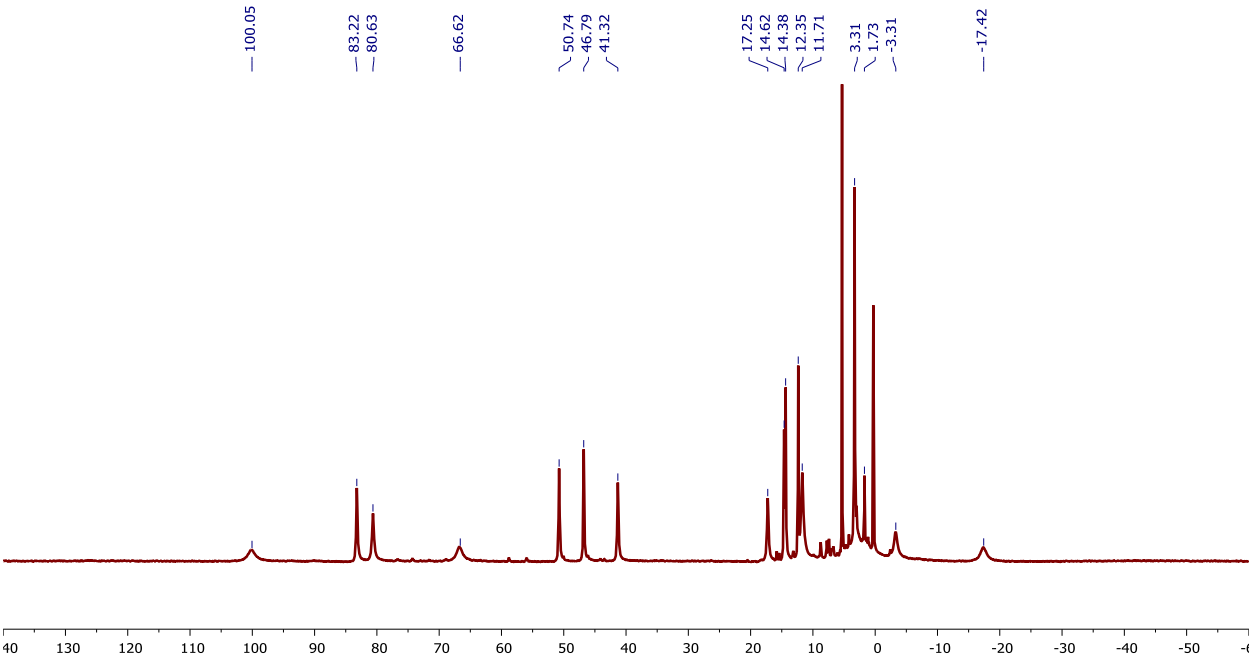


**Figure S11**. $^{1}$H NMR spectrum (300 MHz) of $[LFe_3F(PhPz)_3Fe(NO)][OTf]_2$ (**2-NO**) in $CD_2Cl_2$

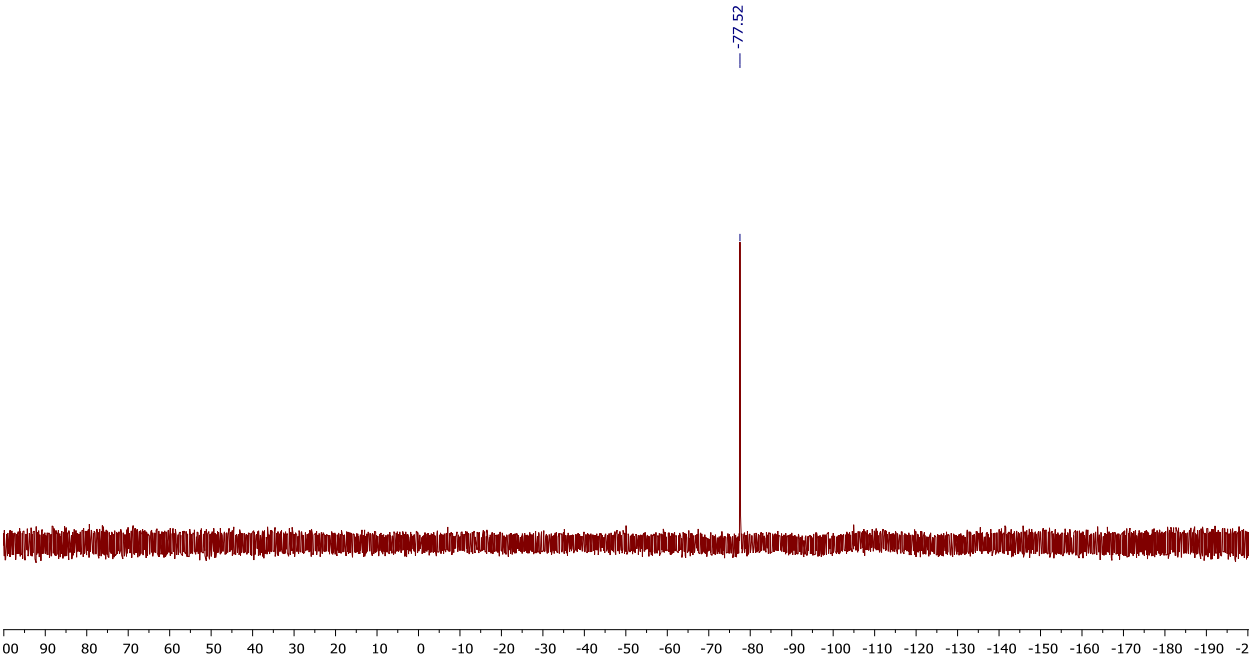


**Figure S12**. $^{19}$F NMR spectrum (300 MHz) of $[LFe_3F(PhPz)_3Fe(NO)][OTf]_2$ (**2-NO**) in $CD_2Cl_2$

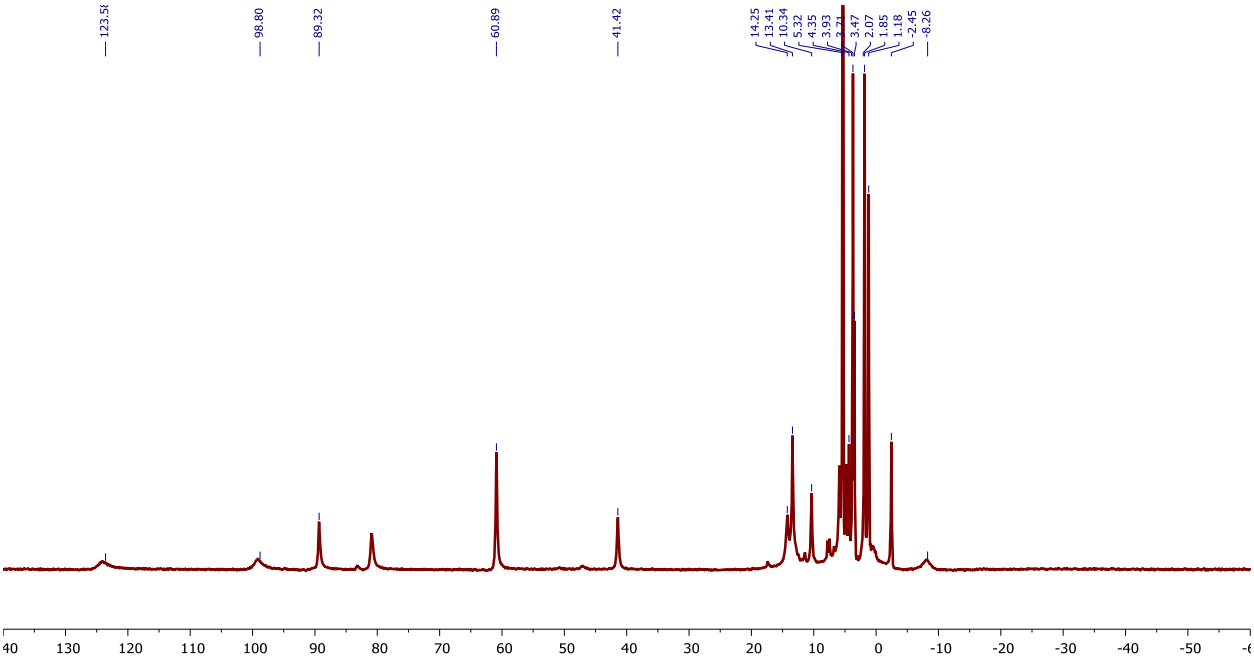


**Figure S13**. $^{1}$H NMR spectrum (300 MHz) of $[LFe_3F(PhPz)_3Fe(NO)][OTf]_3$ (**3-NO**) in $CD_2Cl_2$

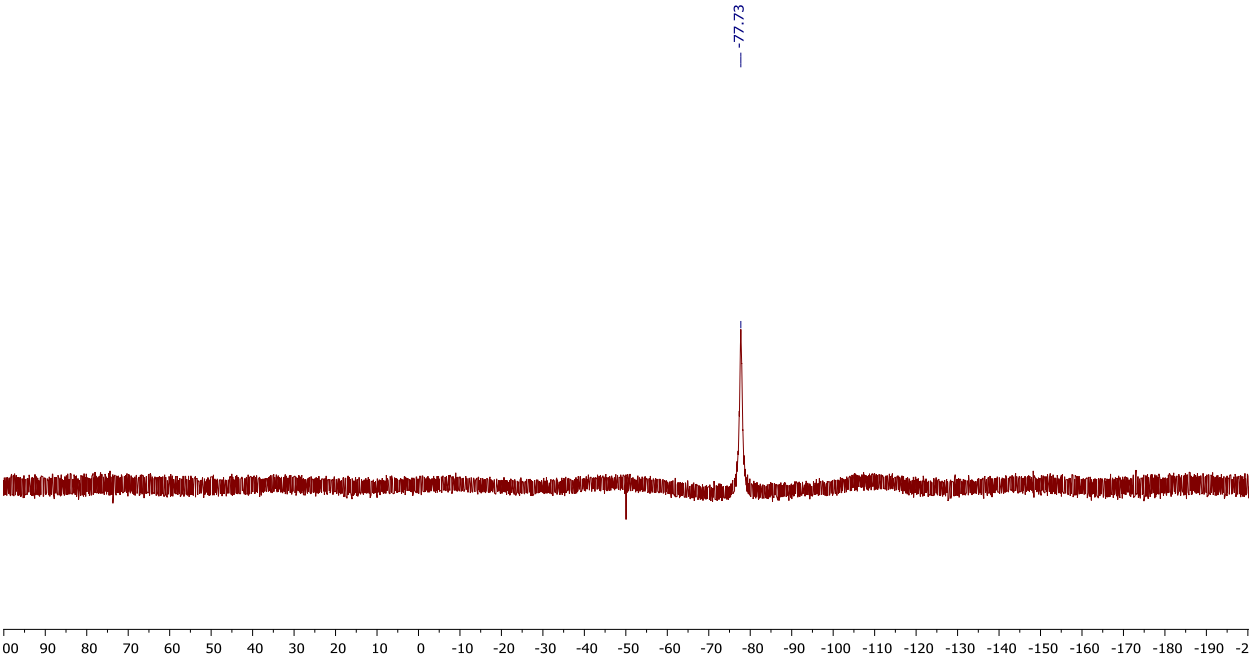


**Figure S14**. $^{19}$F NMR spectrum (300 MHz) of $[LFe_3F(PhPz)_3Fe(NO)][OTf]_3$ (**3-NO**) in $CD_2Cl_2$

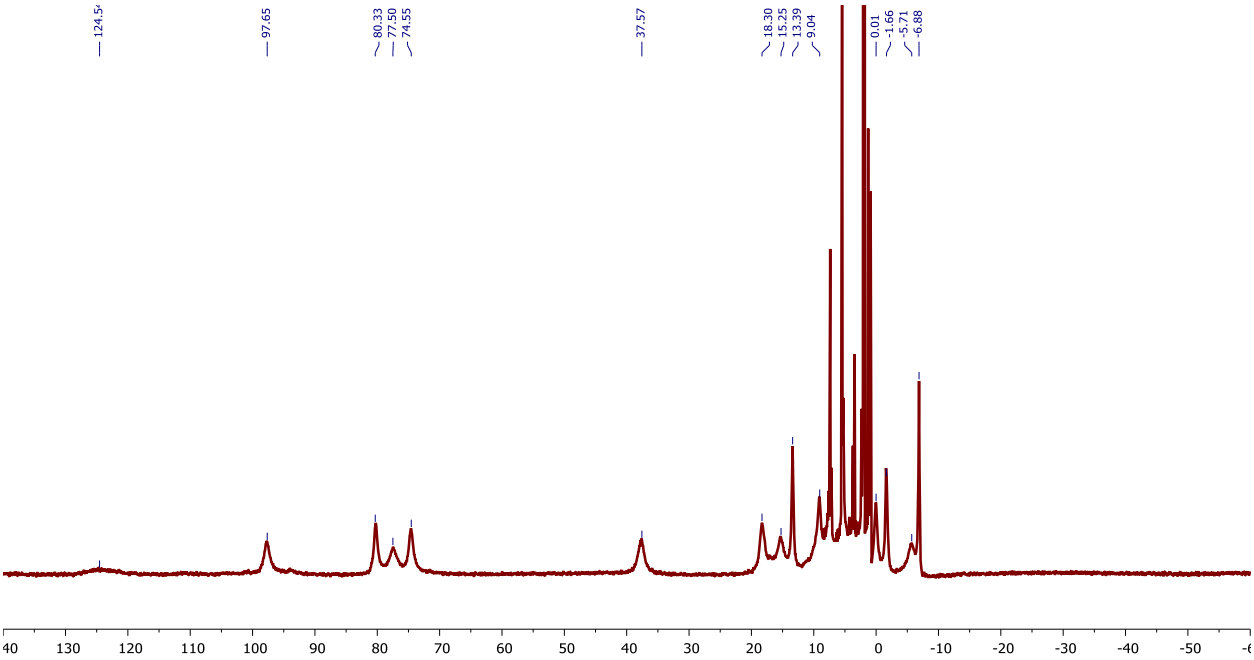


**Figure S15**. $^{1}$H NMR spectrum (300 MHz) of $[LFe_3F(PhPz)_3Fe(NO)][OTf]_3[SbCl_6]$ (**4-NO**) in $CD_3CN$

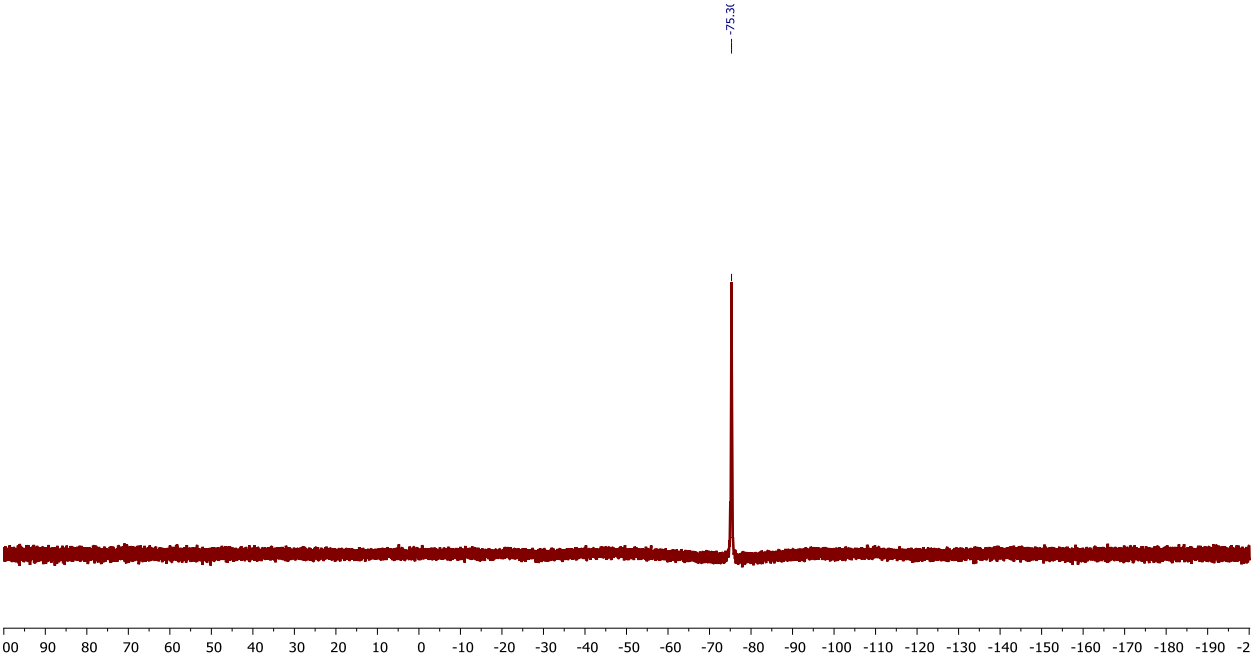


**Figure S16**. $^{19}$F NMR spectrum (300 MHz) of $[LFe_3F(PhPz)_3Fe(NO)][OTf]_3[SbCl_6]$ (**4-NO**) in $CD_3CN$

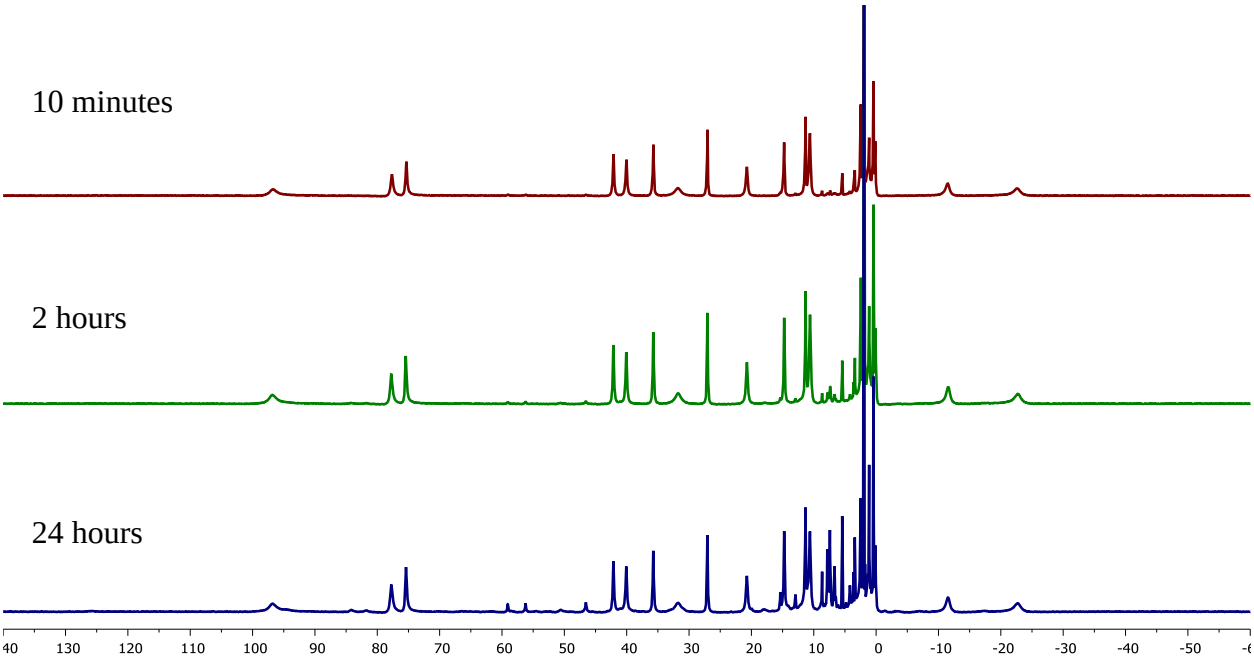


**Figure S17**. $^{1}$H NMR (300 MHz) of reaction mixture of 6 equiv. NO addition to [$LFe_3F(PhPz)_3Fe(NO)$][OTf] (**1-NO**) in $CD_3CN$. The minor species that appears over 24 hours is due to air leakage, as its abundance would change over repeated experiments, it would never completely convert given longer periods of time, and complete conversion would only occur if the reaction was intentionally exposed to air.

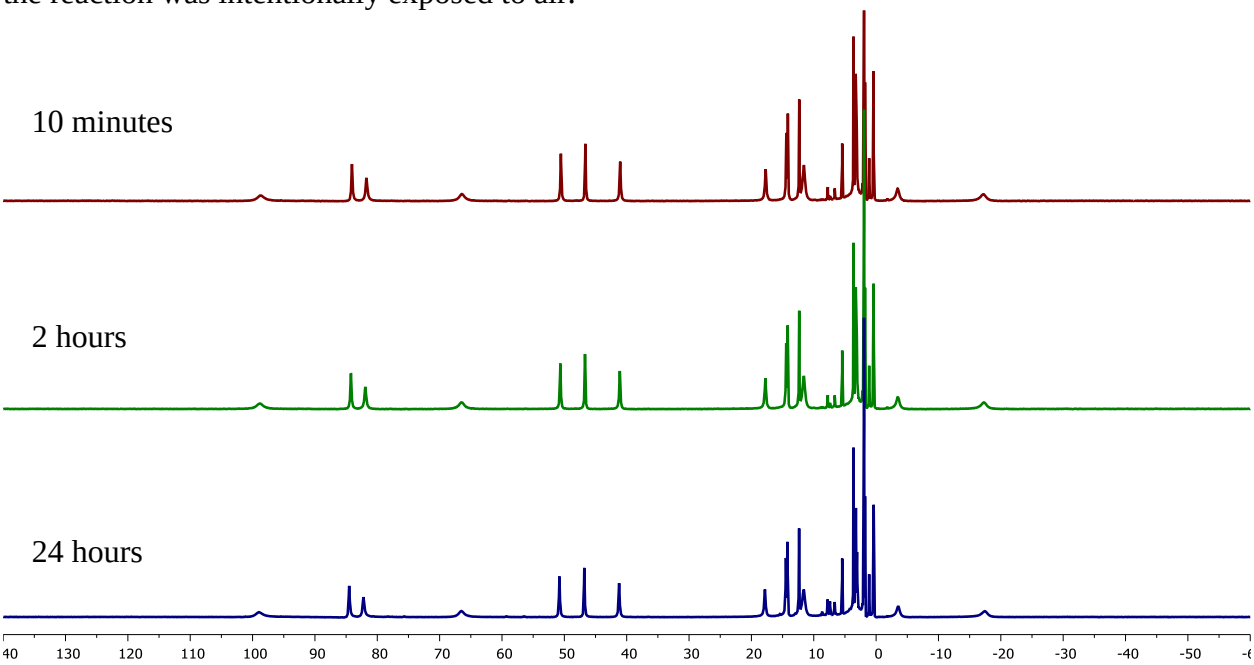


**Figure S18**. $^{1}$H NMR (300 MHz) of reaction mixture of 6 equiv. NO addition to [$LFe_3F(PhPz)_3Fe(NO)$][$OTf]_2$ (**2-NO**) in $CD_3CN$.

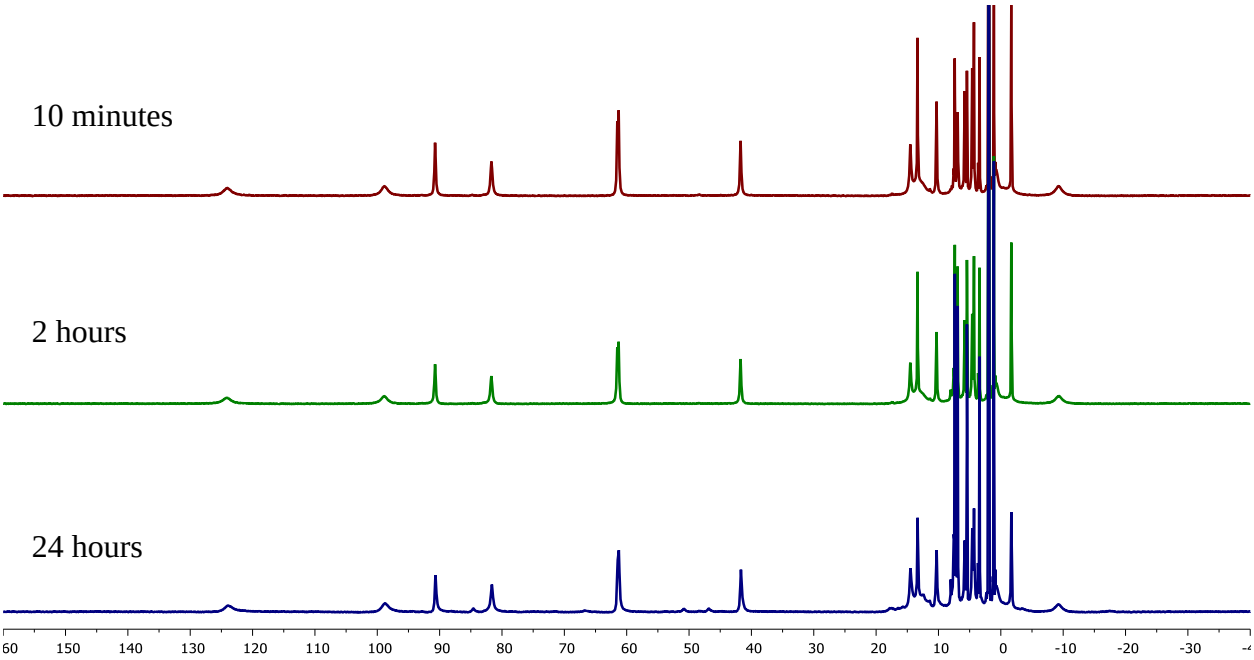


**Figure S19**. $^{1}$H NMR (300 MHz) of reaction mixture of 6 equiv. NO addition to $[LFe_3F(PhPz)_3Fe(NO)][OTf]_3$ (**3-NO**) in $CD_3CN$.

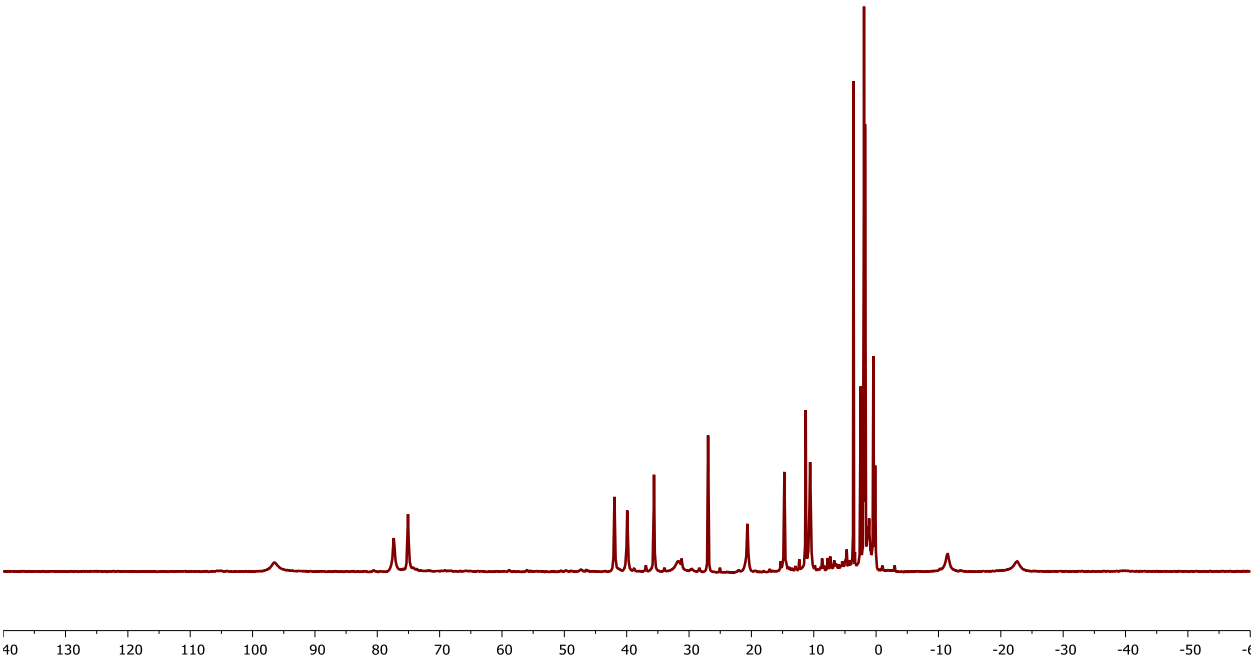


**Figure S20**. $^{1}$H NMR (300 MHz; $CD_3CN$) of reaction mixture of AgOTf addition to $LFe_3F(PhPz)_3Fe(NO)$ (**5-NO**) in thawing THF. The spectrum is identical to $[LFe_3F(PhPz)_3Fe(NO)][OTf]$ (**1-NO**) in $CD_3CN$.

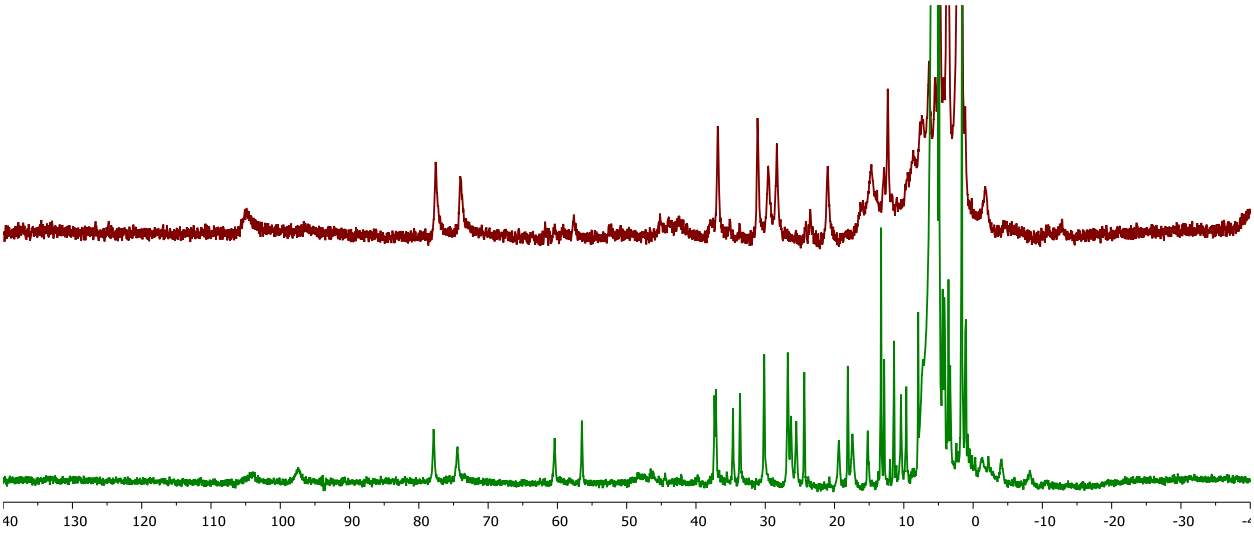


**Figure S21**. (Top) $^{1}$H NMR (300 MHz; $CD_3CN$) of reaction mixture of $LFe_3F(PhPz)_3Fe(NO)$ (**5-NO**) in THF over 24 hours. The spectrum of the major species is identical to $[LFe_3F(PhPz)_3Fe][OTf]$ (**1**) in $CD_3CN$. (Bottom) $^{1}$H NMR (300 MHz; $CD_2Cl_2$) of reaction mixture of $LFe_3F(PhPz)_3Fe(NO)$ (**5-NO**) in THF over 24 hours. The spectrum of the new species is identical to $[LFe_3O(PhPz)_3Fe][OTf]$ $CD_2Cl_2$. We have previously observed decomposition of $LFe_3O(PhPz)_3Fe$ in dichloromethane to the monocationic cluster. This, along with the fact that the $[LFe_3O(PhPz)_3Fe]^+$ cluster is soluble enough in $CD_3CN$ to observe by NMR, we conclude that we can observe formation of a mixture of $[LFe_3F(PhPz)_3Fe]^+$ and $LFe_3O(PhPz)_3Fe$ from the decomposition $LFe_3F(PhPz)_3Fe(NO)$ in THF.

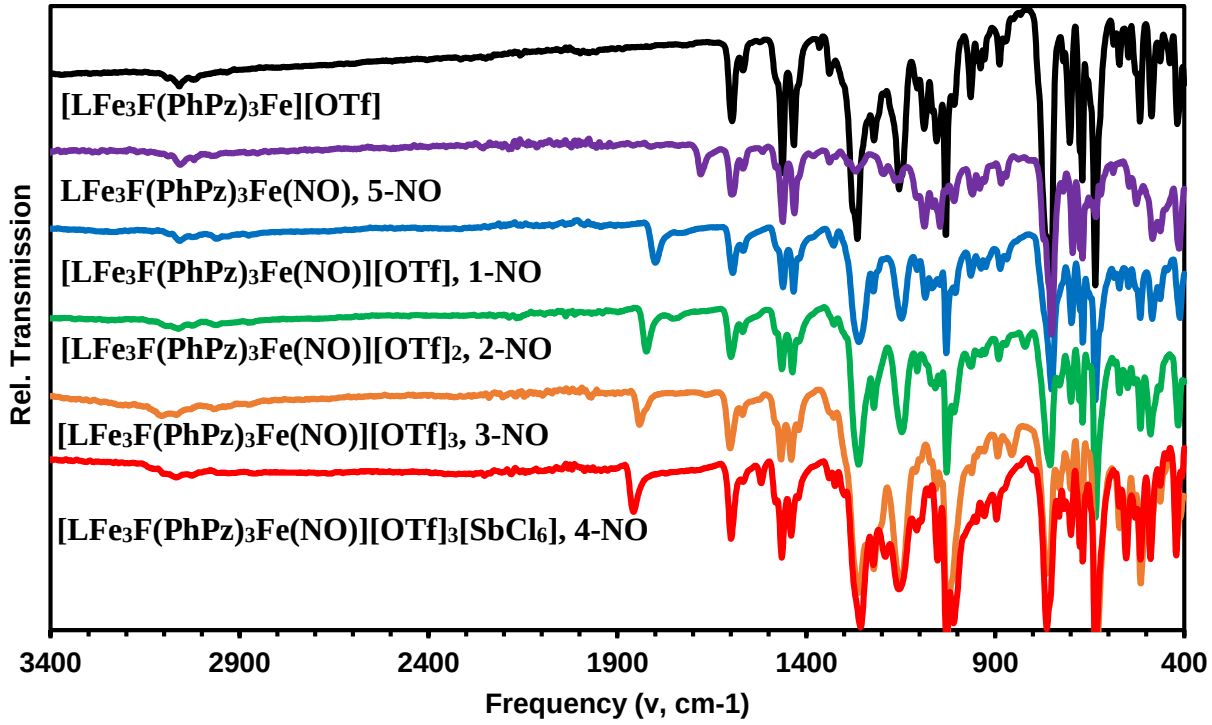


**Figure S22**. Solid state IR spectra of complexes **1**, **1-NO - 5-NO**

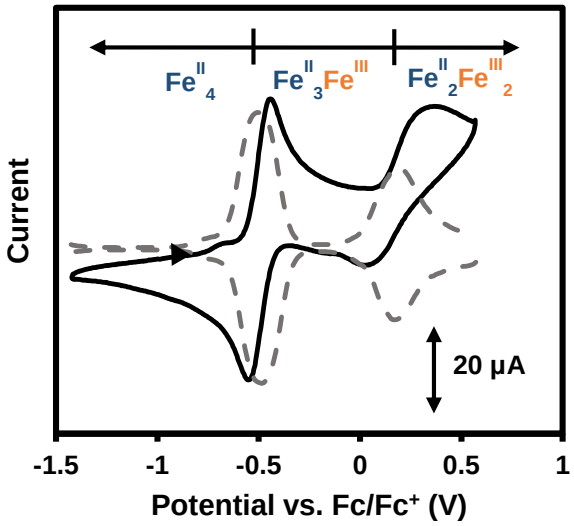


**Figure S23**. Cyclic voltammogram (black trace) of [$LFe_3F(PhPz)_3Fe$][OTf] (**1**; 3 mM) in $CH_3CN$ with 85 mM [$Bu_4N$][$PF_6$] at a scan rate of 200 mV/s with glassy carbon, Pt-wire, and Ag-wire as working, counter, and reference electrode, respectively. Square wave voltammograms (gray dashed trace) overlaid with 0.1 V amplitude, 1.0 s period, and 0.01 V increment.

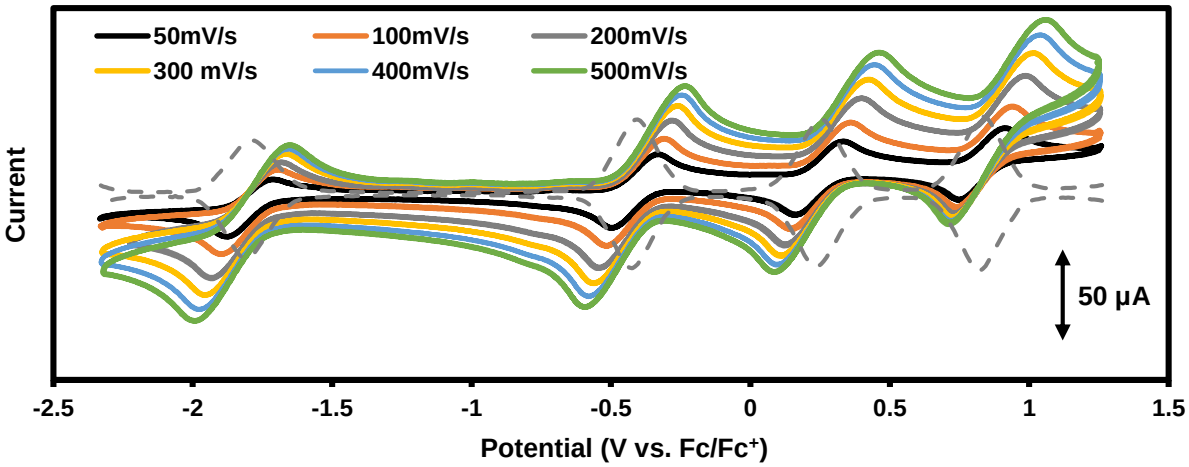


**Figure S24**. Cyclic voltammogram (solid traces) of $[LFe_3F(PhPz)_3Fe(NO)][OTf]$ (**1-NO**; 2 mM) in $CH_2Cl_2$ with 100 mM $[Bu_4N][PF_6]$ at various scan rates with glassy carbon, Pt-wire, and Ag-wire as working, reference, and counter electrode, respectively. Square wave voltammograms (gray dashed trace) overlaid with 0.1 V amplitude, 1.0 s period, and 0.01 V increment. The open circuit potential (OCP) was measured to be -0.7 V.

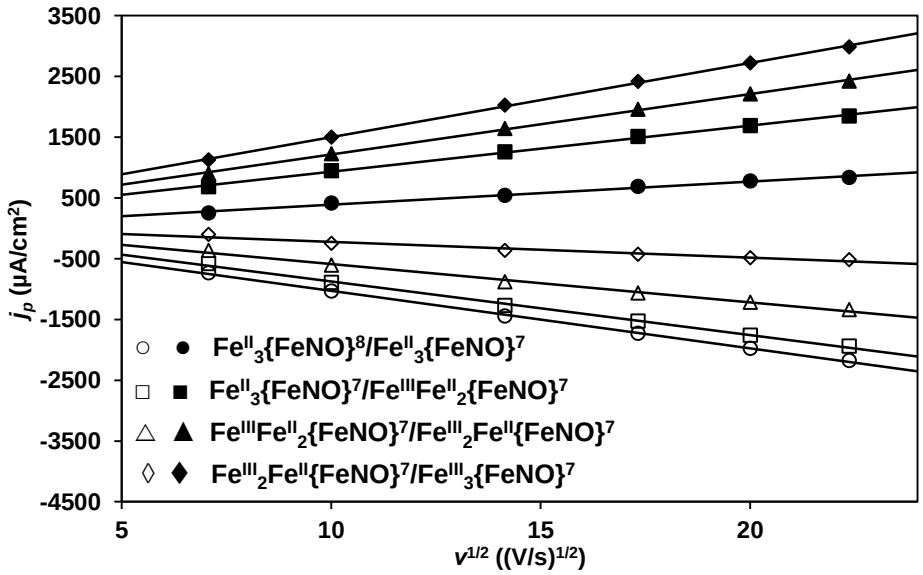


**Figure S25**. Current density ($j_p$) dependence of the square root of the scan rate $\nu^{1/2}$ for the electrochemical events observed in the CV of $[LFe_3F(PhPz)_3Fe(NO)][OTf]$, **1-NO** (Figure S24).

**Mössbauer simulation details for compounds 1 – 3 and 1-NO – 5-NO.** All spectra were simulated as four pairs of symmetric quadrupole doubles with equal populations and Lorentzian lineshipes (the parameter defining the width, Γ, is reported). They were refined to a minimum via least squares optimization (13 fitting parameters per spectrum). Signals appearing above 2 mm/s were indicative with the presence of high-spin $Fe^{II}$ centers and correspond to species with isomer shifts ~ 1 mm/s. The Mössbauer data were fit to be consistent with our previously reported iron clusters.[1] The observed Mossbauer parameters are in agreement with related six-coordinate high-spin $Fe^{II}/Fe^{III}$ centers.[2]

**Simulation details for [LFe$_3$(PhPz)$_3$FFe][OTf] (1):** The Mössbauer spectrum of **1** features an intense signal around 3 mm/s characteristic of a high-spin Fe(II) center. Fitting a quadrupole doublet for this peak led to a model that accounted for ~75% of the overall signal, with a second doublet satisfactorily accounting for the rest of the signal (Figure S29). The final refinement split the 75%-abundant high-spin Fe(II) signal into three equally populated doublets (Figure S30).

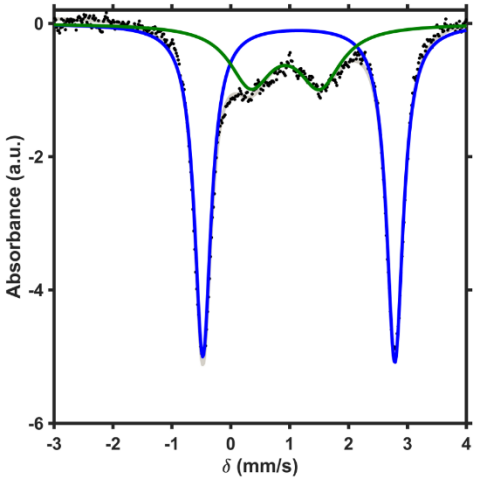


**Figure S26**. Mössbauer spectrum of **1** (black dots) fit with two doublets in ~3:1 ratio refined with parameters: $\delta$ = 1.156 mm/s; $\Delta E_q$ = 3.260 mm/s (blue trace) and $\delta$ = 0.925 mm/s; $\Delta E_q$ = 1.171 mm/s (green trace). The overall fit is the gray trace.

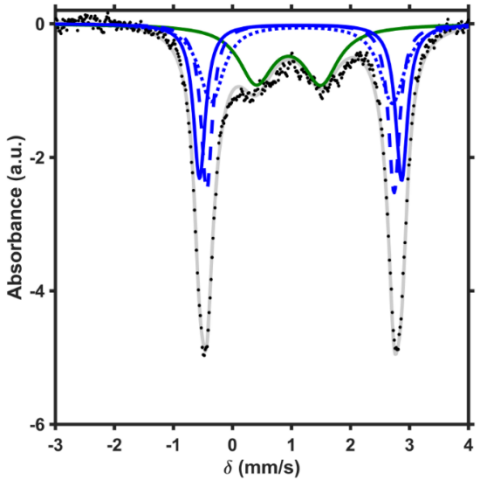


| | δ (mm/s) | $\lvert\Delta E_q\rvert$ (mm/s) | Γ | Rel. % |
|---|---|---|---|---|
| ——— | 1.156 | 3.424 | 0.25 | 25 |
| – – – | 1.152 | 3.176 | 0.23 | 25 |
| ····· | 1.178 | 3.065 | 0.50 | 25 |
| ——— | 0.951 | 1.099 | 0.70 | 25 |

**Figure S27**. Zero applied field $^{57}$Fe Mössbauer spectrum of [$LFe_3F(PhPz)_3Fe$][OTf] (**1**). The data (black dots) was fit to four Fe quadrupole doublets (gray trace). The blue traces represent signals assigned to the high-spin $Fe^{II}$ of the tri-iron core and the green trace is assigned to the apical high-spin $Fe^{II}$.

**Simulation details for [$LFe_3(PhPz)_3FFe$][OTf]$_2$ (2):** The Mössbauer spectrum of **2** was fit by first fitting the signal at 3 mm/s to high-spin Fe(II) (Figure S31A); this fit accounted for ~50% the total spectrum. The remaining spectrum was fit with two nearly equal doublets (Figure S31B); other combinations of this signal to arrive at alternative parameters for these two signals could not be satisfactorily modeled, so these are not included. The final fit split the 50%-abundant Fe(II) signal into two equal doublets (Figure S32).

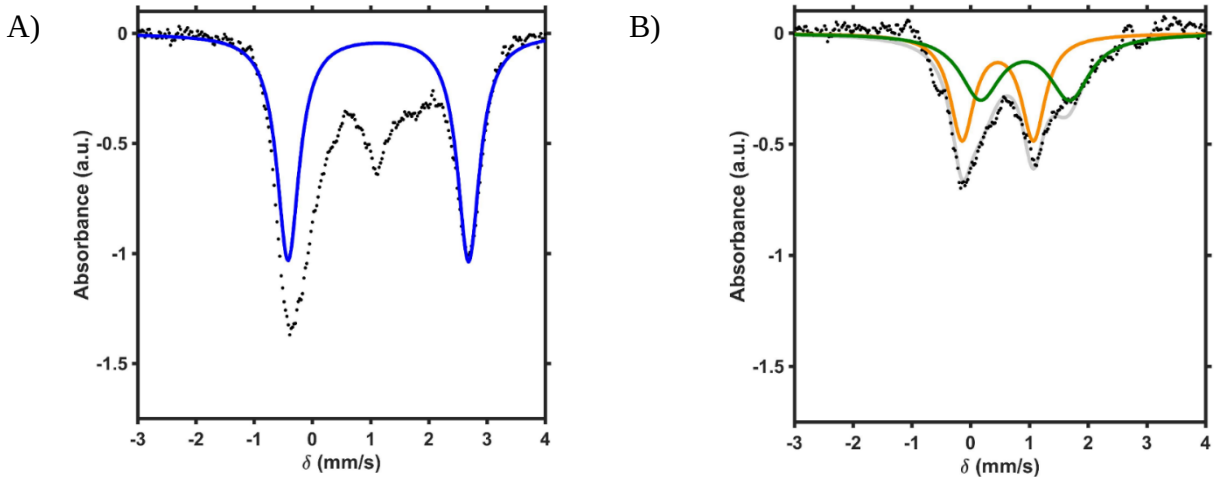


**Figure S28.** Mössbauer spectrum of **2** (black dots) (A) fit with a single doublet refined with parameters consistent with high-spin Fe(II): $\delta$ = 1.132 mm/s; $\Delta E_q$ = 3.101 mm/s (blue trace). (B) Mössbauer spectrum of **2** with this Fe(II) doublet subtracted (black dots) and two equally abundant signals fit (gray trace): $\delta$ = 0.462 mm/s; $\Delta E_q$ = 1.213 mm/s (orange trace), and $\delta$ = 0.928 mm/s; $\Delta E_q$ = 1.522 mm/s (green trace).

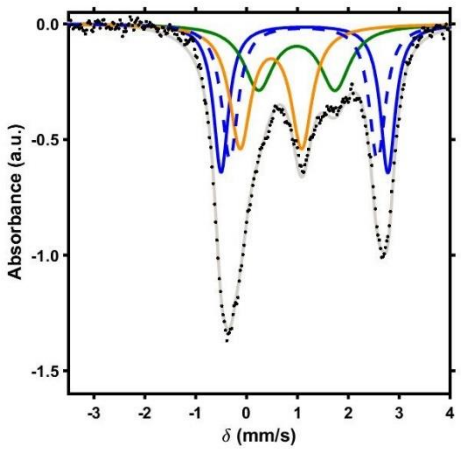


| | δ (mm/s) | $\lvert\Delta E_q\rvert$ (mm/s) | Γ | Rel. % |
|---|---|---|---|---|
| ——— | 1.138 | 3.297 | 0.35 | 25 |
| – – – | 1.122 | 2.899 | 0.39 | 25 |
| ——— | 0.479 | 1.211 | 0.50 | 29 |
| ——— | 0.987 | 1.504 | 0.70 | 21 |

**Figure S29**. Zero applied field $^{57}$Fe Mössbauer spectrum of $[LFe_3F(PhPz)_3Fe][OTf]_2$ (**2**). The data (black dots) was fit to four Fe quadrupole doublets (gray trace). The blue traces represent signals assigned to the high-spin $Fe^{II}$ of the tri-iron core, the orange trace is assigned to high-spin $Fe^{III}$ in the tri-iron core, and the green trace is assigned to the apical high-spin $Fe^{II}$. The best fit was obtained by having a slight deviation from four equally abundant Fe centers.

**Simulation details for $[LFe_3(PhPz)_3FFe(CH_3CN)][OTf]_3$ (3):** The Mössbauer spectrum of **3** contains three easily observable features, which was first approximated by fitting two doublets (Figure S33A). This fit shows inadequate modeling for the signal around 2 mm/s, so a third doubled was modeled in (Figure S33B-D). This fit led to three signals in an approximately 1:1:2 ratios. Of the possible distribution of these three signals, the fit in Figure S33D is favored, because it has isomer shifts self-consistent for the two Fe(III) centers (0.4 – 0.5 mm/s) and the Fe(II) center (1.00 – 1.15 mm/s) of the 'tri-iron' core of our related iron clusters presented here and previously reported. Furthermore, the third signal is most consistent with a high-spin five-coordinate Fe(II) (~0.1 mm/s lower than the corresponding six-coordinate Fe(II) signal), which is in agreement of the coordination of the apical Fe(II) in the crystal structure of **3** (Figure S). The final fit was refined by splitting the 50%-abundant Fe(III) signal into two equal signals (Figure S34).

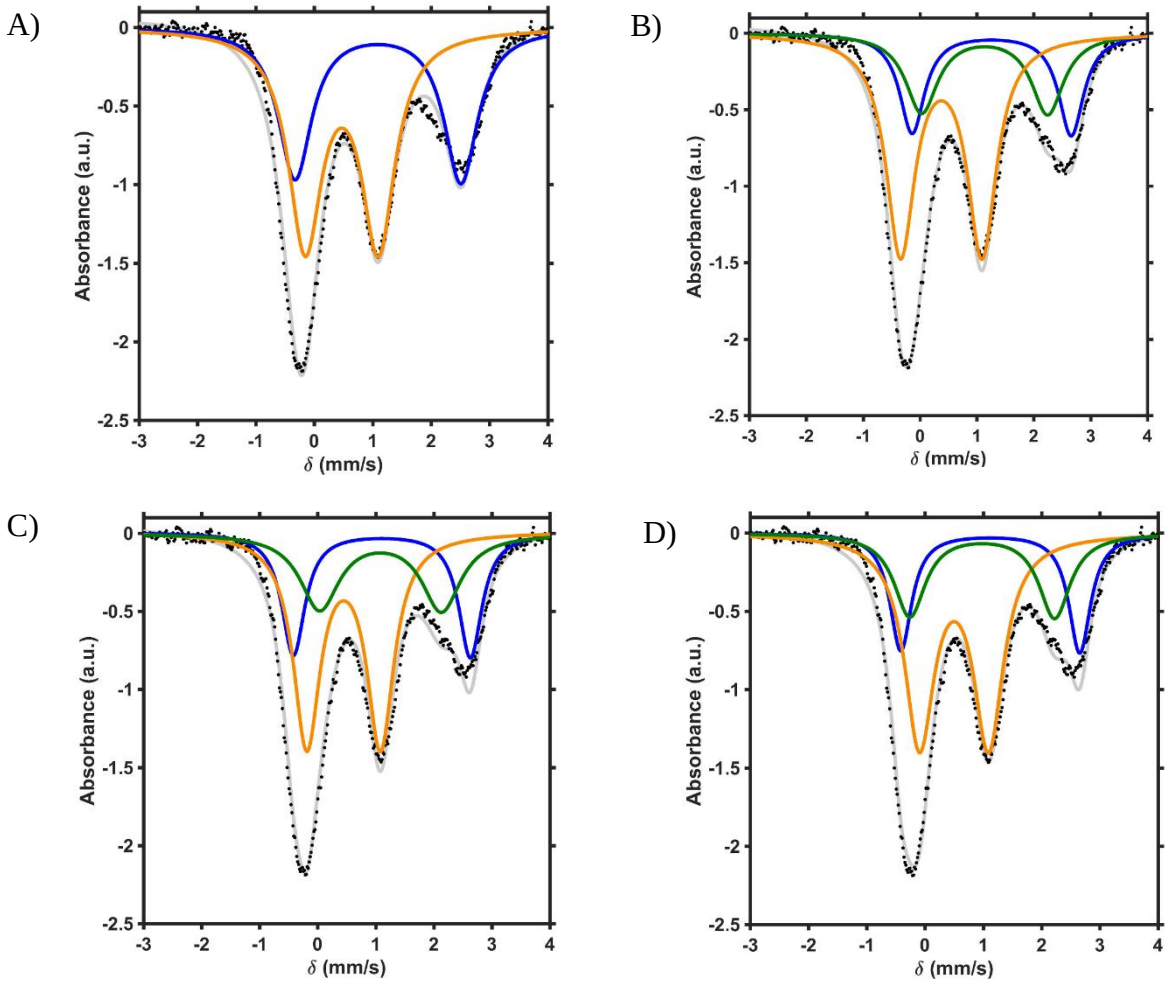

**Figure S30.** Mössbauer spectrum of **3** (black dots) (A) fit with two signals (gray trace) refined with parameters: $\delta$ = 1.091 mm/s; $\Delta E_q$ = 2.841 mm/s (blue trace), and $\delta$ = 0.471 mm/s; $\Delta E_q$ = 1.253 mm/s (orange trace). (B) Mössbauer spectrum of **3** fit with three signals in a 1:1:2 ratio (gray trace) with the parameters: $\delta$ = 1.261 mm/s; $\Delta E_q$ = 2.797 mm/s (blue trace), $\delta$ = 1.137 mm/s; $\Delta E_q$ = 2.216 mm/s (green trace), and $\delta$ = 0.374 mm/s; $\Delta E_q$ = 1.433 mm/s (orange trace). (C) Mössbauer spectrum of **3** fit with three signals in a 1:1:2 ratio (gray trace) with the parameters: $\delta$ = 1.106 mm/s; $\Delta E_q$ = 3.050mm/s (blue trace), $\delta$ = 1.083 mm/s; $\Delta E_q$ = 2.098 mm/s (green trace), and $\delta$ = 0.447 mm/s; $\Delta E_q$ = 1.269 mm/s (orange trace). (D) Mössbauer spectrum of **3** fit with three signals in a 1:1:2 ratio (gray trace) with the parameters: $\delta$ = 1.120 mm/s; $\Delta E_q$ = 3.071 mm/s (blue trace), $\delta$ = 0.981 mm/s; $\Delta E_q$ = 2.486 mm/s (green trace), and $\delta$ = 0.498 mm/s; $\Delta E_q$ = 1.186 mm/s (orange trace).

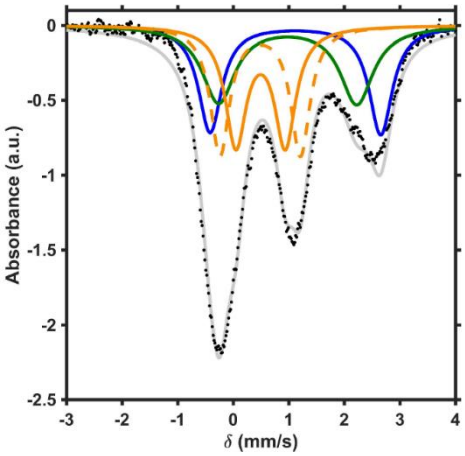


| | δ (mm/s) | $\lvert\Delta E_q\rvert$ (mm/s) | Γ | Rel. % |
|---|---|---|---|---|
| ——— | 1.120 | 3.071 | 0.51 | 25 |
| ——— | 0.492 | 0.889 | 0.46 | 25 |
| – – – | 0.487 | 1.449 | 0.42 | 25 |
| ——— | 0.981 | 2.486 | 0.72 | 25 |

**Figure S31**. Zero applied field $^{57}$Fe Mössbauer spectrum of $[LFe_3F(PhPz)_3Fe(CH_3CN)][OTf]_3$ (**3**). The data (black dots) was fit to four Fe quadrupole doublets (gray trace). The blue trace represents the signal assigned to the high-spin $Fe^{II}$ of the tri-iron core, the orange traces are assigned to high-spin $Fe^{III}$ in the tri-iron core, and the green trace is assigned to the apical high-spin $Fe^{II}$.

**Simulation details for $LFe_3(PhPz)_3FFe(NO)$ (5-NO):** The Mössbauer spectrum of **5-NO** displays three readily distinguished signals. The major two were initially fit with a single doublet, which had parameters consistent with high-spin Fe(II) (Figure S35); the remaining signal was fit in a 3:1 ratio relative to the first signal. The final fit split the high-spin Fe(II) doublet into three equal doublets (Figure S36).

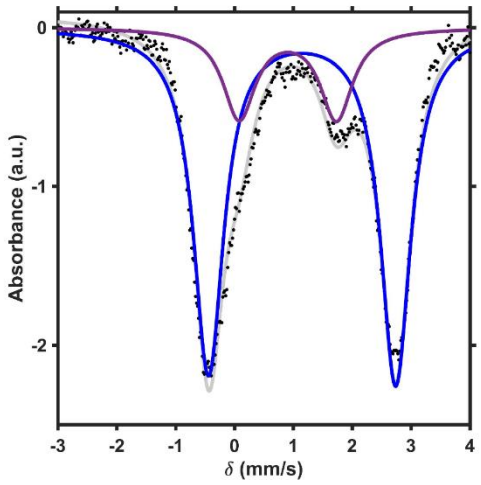


**Figure S32.** Mössbauer spectrum of **5-NO** (black dots) fit with two doublets in a ~3:1 ratio (gray trace) with the parameters: $\delta$ = 1.149 mm/s; $\Delta E_q$ = 3.177 mm/s (blue trace), and $\delta$ = 0.906 mm/s; $\Delta E_q$ = 1.651 mm/s (purple trace).

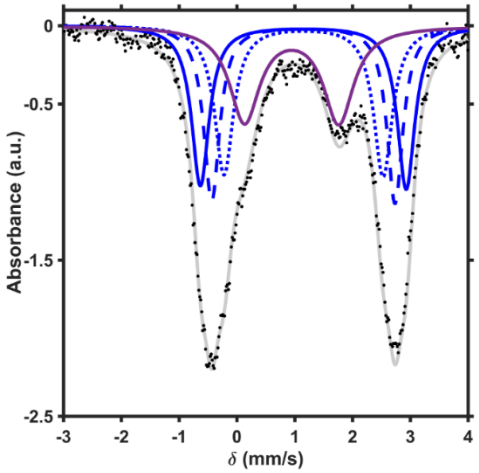


| | δ (mm/s) | $\lvert\Delta E_q\rvert$ (mm/s) | Γ | Rel. % |
|---|---|---|---|---|
| ——— | 1.148 | 3.561 | 0.37 | 25 |
| – – – | 1.150 | 3.172 | 0.33 | 25 |
| ····· | 1.153 | 2.753 | 0.39 | 25 |
| ——— | 0.947 | 1.629 | 0.63 | 25 |

**Figure S33**. Zero applied field $^{57}$Fe Mössbauer spectrum of $LFe_3F(PhPz)_3Fe(NO)$ (**5-NO**). The data (black dots) was fit to four Fe quadrupole doublets (gray trace). The blue traces represent the signal assigned to the high-spin $Fe^{II}$ of the tri-iron core and the purple trace is assigned to the apical $\{FeNO\}^8$.

**Simulation details for [LFe$_3$(PhPz)$_3$FFe(NO)][OTf] (1-NO):** The Mössbauer spectrum of **1-NO** contains four distinguishable signals (one being a shoulder on the peak below 0 mm/s). These four signals were fit to two doublets based on their relative intensities and had an approximate 3:1 ratio (Figure S37). The final fit refined the intense Fe(II) doublet into three equal signals (Figure S38).

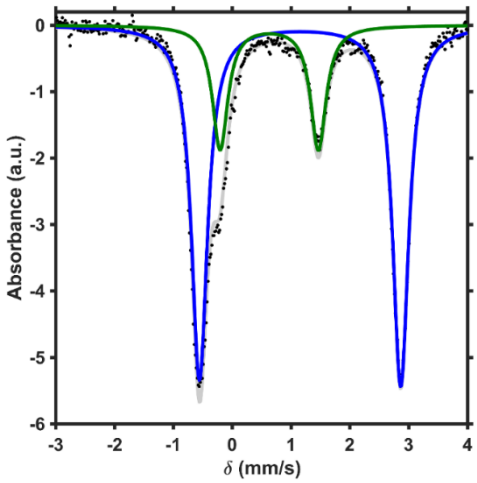


**Figure S34.** Mössbauer spectrum of **1-NO** (black dots) fit with two doublets in a ~3:1 ratio (gray trace) with the parameters: $\delta$ = 1.139 mm/s; $\Delta E_q$ = 3.308 mm/s (blue trace), and $\delta$ = 0.609 mm/s; $\Delta E_q$ = 1.631 mm/s (green trace).

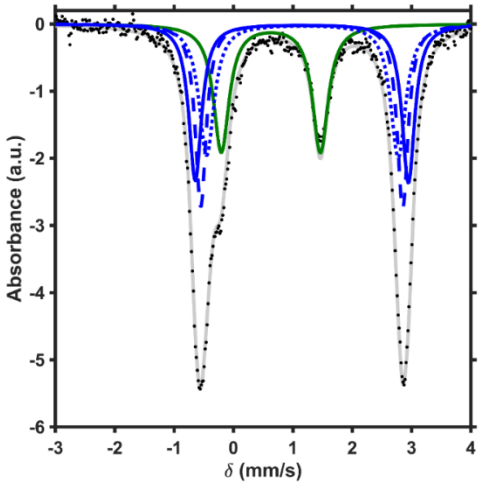


| | δ (mm/s) | $\lvert\Delta E_q\rvert$ (mm/s) | Γ | Rel. % |
|---|---|---|---|---|
| ——— | 1.152 | 3.592 | 0.26 | 25 |
| – – – | 1.150 | 3.403 | 0.22 | 25 |
| ····· | 1.162 | 3.229 | 0.31 | 25 |
| ——— | 0.630 | 1.669 | 0.32 | 25 |

**Figure S35**. Zero applied field $^{57}$Fe Mössbauer spectrum of [LFe$_3$F(PhPz)$_3$Fe(NO)][OTf] (**1-NO**). The data (black dots) was fit to four Fe quadrupole doublets (gray trace). The blue traces represent the signal assigned to the high-spin Fe$^{II}$ of the tri-iron core and the green trace is assigned to the apical {FeNO}$^7$.

**Simulation details for [LFe$_3$(PhPz)$_3$FFe(NO)][OTf]$_2$ (2-NO):** The Mössbauer spectrum of **2-NO** displays four readily-distinguished signals. The signal above 3 mm/s was initially fit as high-spin Fe(II), and this doublet accounts for 50% of the overall spectrum (Figure S39A). The remaining signal was fit as two equally abundant doublets in three different ways (Figures S39B-D). The fit in Figure S39B gives unreasonable isomer shifts of -0.1 and 0.2 mm/s (orange and green traces, respectively). The fits in Figures S39C and S39D are only slightly different, but the fit in Figure S39D gives parameters that are more self-consistent with isomer shift values for the Fe(III) center of the 'tri-iron core' (0.4 mm/s; orange trace) and the {FeNO}$^7$ center of the fluoride-bridged tetranuclear iron clusters (0.6 mm/s; green trace; see parameter refinement for **1-NO**). The final fit split the 50%-abundant Fe(II) signal into two doublets (Figure S40).

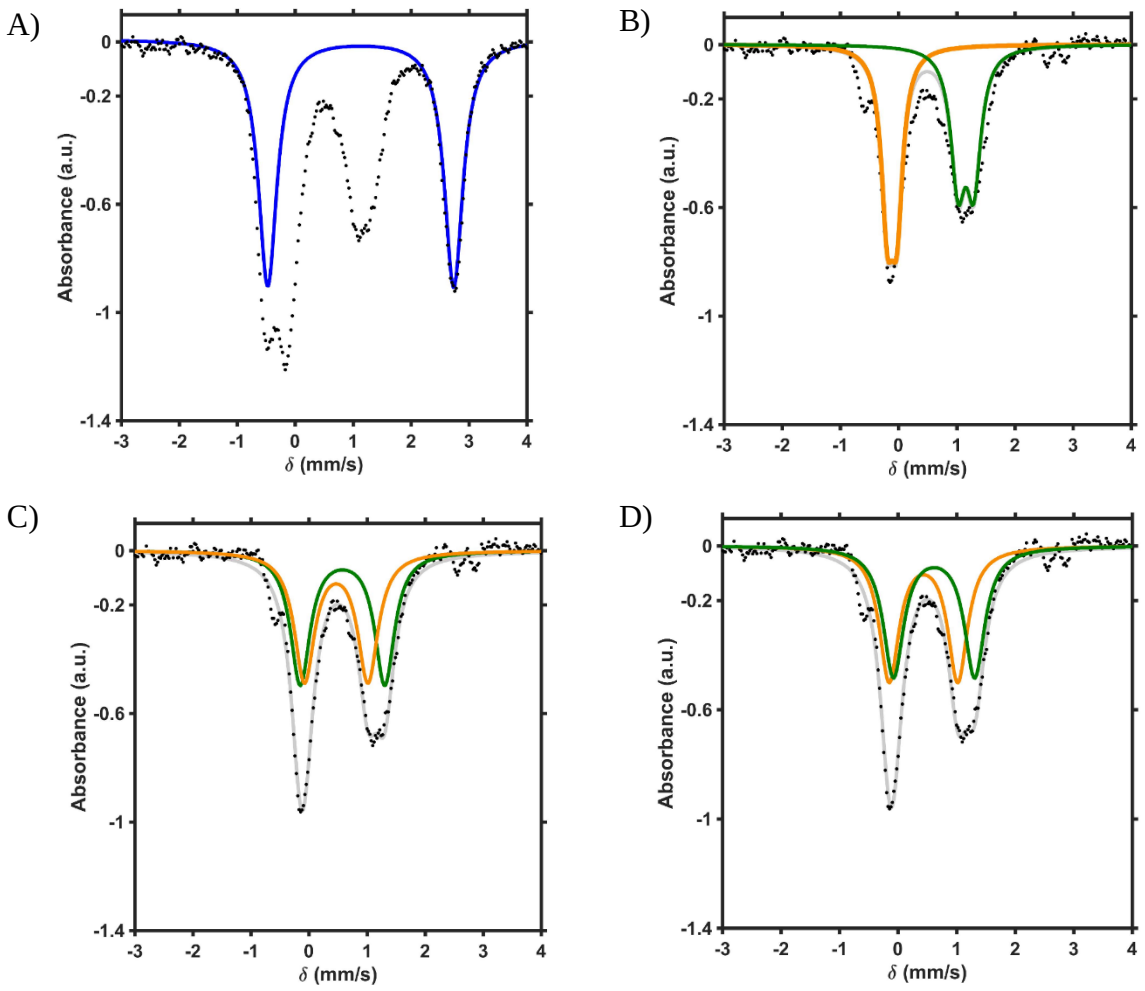


**Figure S36.** Mössbauer spectrum of **2-NO** (black dots) (A) fit with a single doublet refined with parameters consistent with high-spin Fe(II): $\delta$ = 1.132 mm/s; $\Delta E_q$ = 3.211 mm/s (blue trace). (B) Mössbauer spectrum of **2-NO** with this Fe(II) doublet subtracted (black dots) and two equally abundant signals fit (gray trace): $\delta$ = -0.111 mm/s; $\Delta E_q$ = 0.165 mm/s (orange trace), and $\delta$ = 1.158 mm/s; $\Delta E_q$ = 0.270 mm/s (green trace). (C) Mössbauer spectrum of **2-NO** with this Fe(II) doublet subtracted (black dots) and two equally abundant signals fit (gray trace): $\delta$ = 0.577 mm/s; $\Delta E_q$ = 1.456 mm/s (green trace), and $\delta$ = 0.469 mm/s; $\Delta E_q$ = 1.094 mm/s (orange trace).

(D) Mössbauer spectrum of **2-NO** with this Fe(II) doublet subtracted (black dots) and two equally abundant signals fit (gray trace): $\delta$ = 0.616 mm/s; $\Delta E_q$ = 1.387 mm/s (green trace), and $\delta$ = 0.435 mm/s; $\Delta E_q$ = 1.171 mm/s (orange trace).

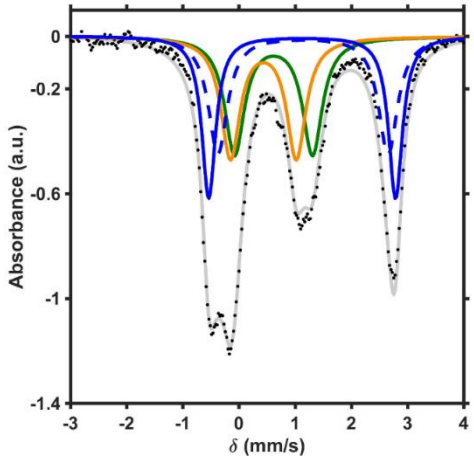


| | δ (mm/s) | $\lvert\Delta E_q\rvert$ (mm/s) | Γ | Rel. % |
|---|---|---|---|---|
| ——— | 1.121 | 3.309 | 0.30 | 25 |
| – – – | 1.150 | 3.026 | 0.46 | 25 |
| ——— | 0.435 | 1.171 | 0.41 | 25 |
| ——— | 0.616 | 1.387 | 0.42 | 25 |

**Figure S37**. Zero applied field $^{57}$Fe Mössbauer spectrum of $[LFe_3F(PhPz)_3Fe(NO)][OTf]_2$ (**2-NO**). The data (black dots) was fit to four Fe quadrupole doublets (gray trace). The blue traces represent the signal assigned to the high-spin $Fe^{II}$ of the tri-iron core, the orange trace is assigned to the high-spin $Fe^{III}$ in the tri-iron core, and the green trace is assigned to the apical $\{FeNO\}^7$.

**Simulation details for $[LFe_3(PhPz)_3FFe(NO)][OTf]_3$ (3-NO):** The Mössbauer spectrum of **3-NO** displays three major features (instead of the expected eight for four Fe centers). The peak around 3 mm/s was modeled as a high-spin Fe(II) with parameters consistent with other Fe(II) centers in the 'tri-iron core' of the tetranuclear clusters; this fit accounted for 25% of the total signal (Figure S41A). Subtracting this doublet from the data, the remaining signal could be fit reasonably well with either one or two equally abundant quadrupole doublets (Figures S41B and S41C), however these fits were ruled out since they were inconsistent with our crystallographic analysis of **3-NO**. There are many possible ways to fit 3 doublets in this residual signal; below are shown three fits that give reasonable fit parameters for two high-spin Fe(III) centers and a high-spin five-coordinate $\{FeNO\}^7$ (Figure S41D-F). The fit in Figure S41F gave parameters the most self-consistent within this series of clusters, and was used for the final refinement (Figure S42).

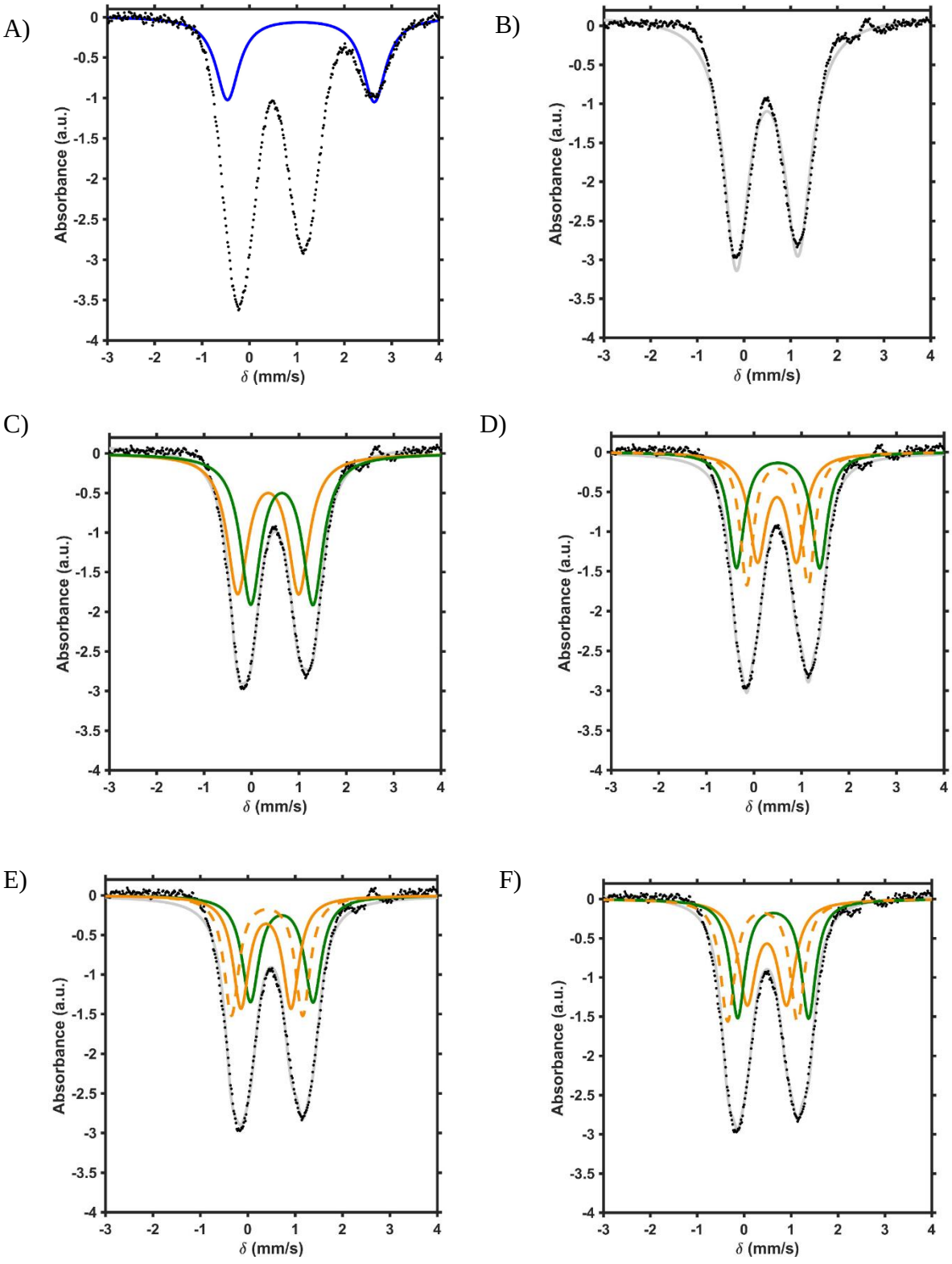


**Figure S38.** Mössbauer spectrum of **3-NO** (black dots) (A) fit with a single doublet refined with parameters consistent with high-spin Fe(II): $\delta$ = 1.087 mm/s; $\Delta E_q$ = 3.100 mm/s (blue trace). (B) Mössbauer spectrum of **3-NO** with this Fe(II) doublet subtracted (black dots) and fit with a

single quadrupole doublet (gray trace): $\delta$ = 0.501 mm/s; $\Delta E_q$ = 1.319 mm/s. (C) Mössbauer spectrum of **3-NO** with this Fe(II) doublet subtracted (black dots) and two equally abundant signals fit (gray trace): $\delta$ = 0.354 mm/s; $\Delta E_q$ = 1.291 mm/s (orange trace), and $\delta$ = 0.643 mm/s; $\Delta E_q$ = 1.314 mm/s (green trace). (D) Mössbauer spectrum of **3-NO** with this Fe(II) doublet subtracted (black dots) and three equally abundant signals fit (gray trace): $\delta$ = 0.488 mm/s; $\Delta E_q$ = 0.819 mm/s (solid orange trace), and $\delta$ = 0.499 mm/s; $\Delta E_q$ = 1.292 mm/s (dashed orange trace), and $\delta$ = 0.512 mm/s; $\Delta E_q$ = 1.750 mm/s (green trace). (E) Mössbauer spectrum of **3-NO** with this Fe(II) doublet subtracted (black dots) and three equally abundant signals fit (gray trace): $\delta$ = 0.387 mm/s; $\Delta E_q$ = 1.058 mm/s (solid orange trace), and $\delta$ = 0.409 mm/s; $\Delta E_q$ = 1.503 mm/s (dashed orange trace), and $\delta$ = 0.719 mm/s; $\Delta E_q$ = 1.321 mm/s (green trace). (F) Mössbauer spectrum of **3-NO** with this Fe(II) doublet subtracted (black dots) and three equally abundant signals fit (gray trace): $\delta$ = 0.486 mm/s; $\Delta E_q$ = 0.840 mm/s (solid orange trace), and $\delta$ = 0.395 mm/s; $\Delta E_q$ = 1.486 mm/s (dashed orange trace), and $\delta$ = 0.620 mm/s; $\Delta E_q$ = 1.512 mm/s (green trace).

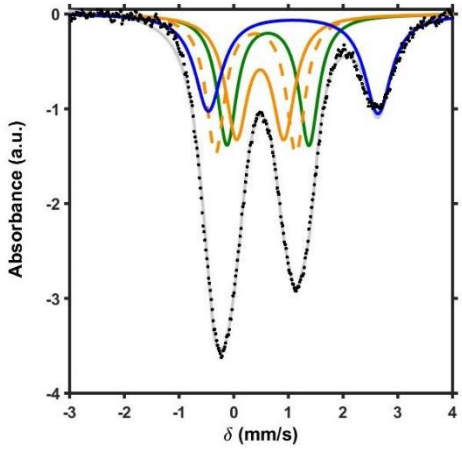


| | δ (mm/s) | $\lvert\Delta E_q\rvert$ (mm/s) | Γ | Rel. % |
|---|---|---|---|---|
| | 1.087 | 3.100 | 0.59 | 25 |
| | 0.484 | 0.868 | 0.49 | 25 |
| | 0.402 | 1.471 | 0.41 | 25 |
| | 0.615 | 1.507 | 0.44 | 25 |

**Figure S39**. Zero applied field $^{57}$Fe Mössbauer spectrum of $[LFe_3F(PhPz)_3Fe(NO)][OTf]_3$ (**3-NO**). The data (black dots) was fit to four Fe quadrupole doublets (gray trace). The blue trace represents the signal assigned to the high-spin $Fe^{II}$ of the tri-iron core, the orange traces are assigned to the high-spin $Fe^{III}$ in the tri-iron core, and the green trace is assigned to the apical $\{FeNO\}^7$.

**Simulation details for $[LFe_3(PhPz)_3FFe(NO)][OTf]_3[SbCl_6]$ (4-NO):** The Mössbauer spectrum of **4-NO** displays two broad features, which were adequately fit as a single quadrupole doublet (Figure S43). Since it is likely that the Fe(III) signals are overlapping with the $\{FeNO\}^7$ signal (see Mössbauer spectra of **2-NO** and **3-NO**), modeling the four separate Fe centers is not included. This spectra is consistent, however, with our assignment of **4-NO** as a cluster containing no Fe(II) centers, since there the characteristic signal around 3 mm/s is absent.

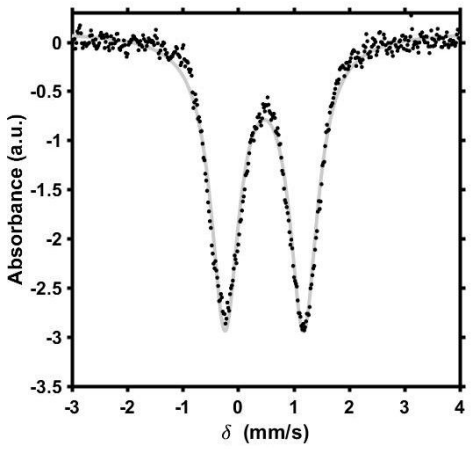


| | δ (mm/s) | $\|\Delta E_q\|$ (mm/s) | Γ | Rel. % |
|---|---|---|---|---|
| ——— | 0.471 | 1.420 | 0.61 | 100 |

**Figure S40**. Zero applied field $^{57}$Fe Mössbauer spectrum of $[LFe_3F(PhPz)_3Fe(NO)][OTf]_3[SbCl_6]$ (**4-NO**). The data (black dots) was fit to a single Fe quadrupole doublet (gray trace). We postulate that the signal for the apical $\{FeNO\}^7$ is overlapping with the doublet(s) for the high-spin Fe(III) in the 'tri-iron core'.

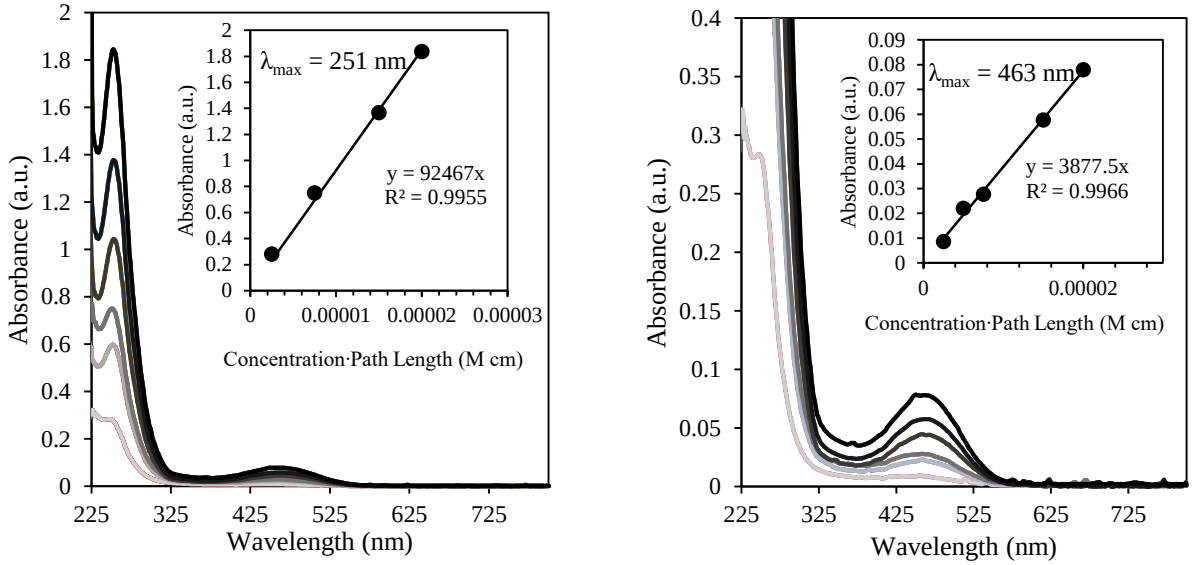


**Figure S41**. UV-Vis spectra of $[LFe_3F(PhPz)_3Fe][OTf]$ (**1**) in $CH_2Cl_2$

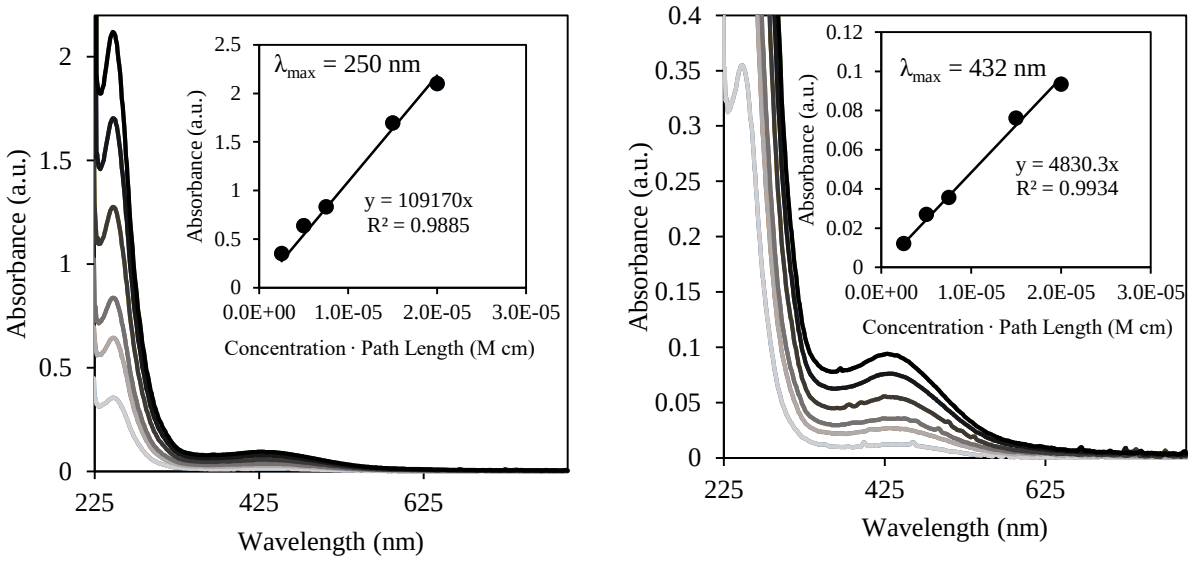


**Figure S42**. UV-Vis spectra of $[LFe_3F(PhPz)_3Fe][OTf]_2$ (**2**) in $CH_2Cl_2$

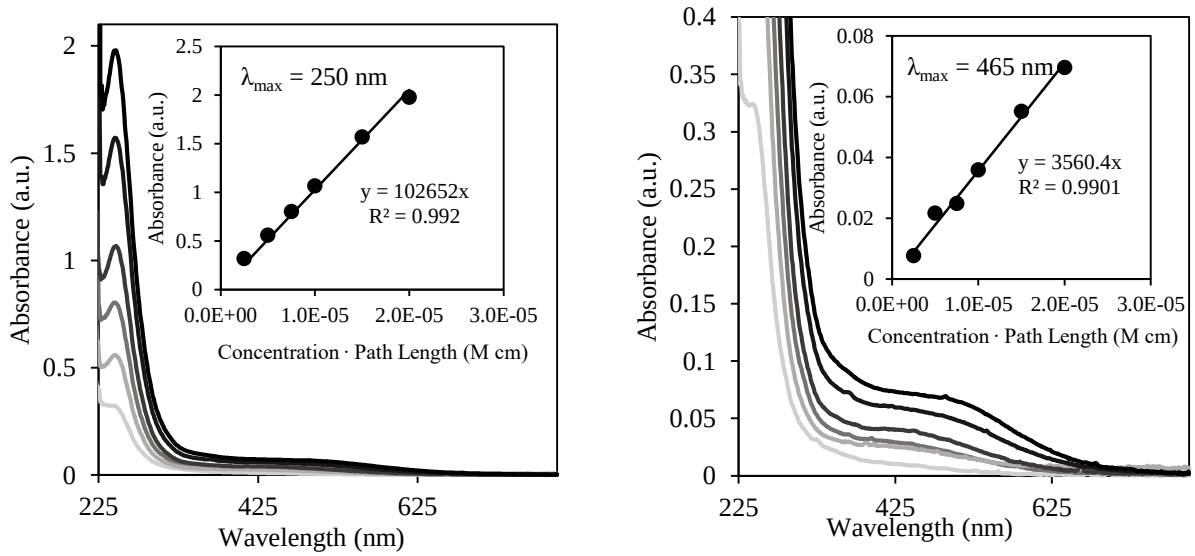


**Figure S43**. UV-Vis spectra of $[LFe_3F(PhPz)_3Fe(CH_3CN)][OTf]_3$ (**3**) in $CH_2Cl_2$

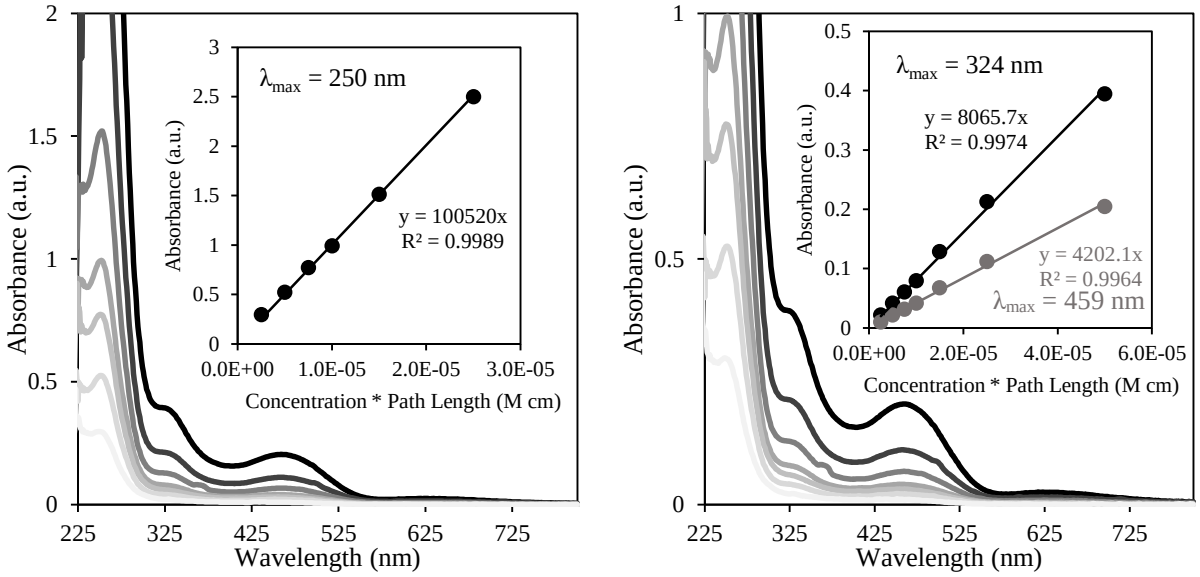


**Figure S44**. UV-Vis spectra of $[LFe_3F(PhPz)_3Fe(NO)][OTf]$ (**1-NO**) in $CH_2Cl_2$

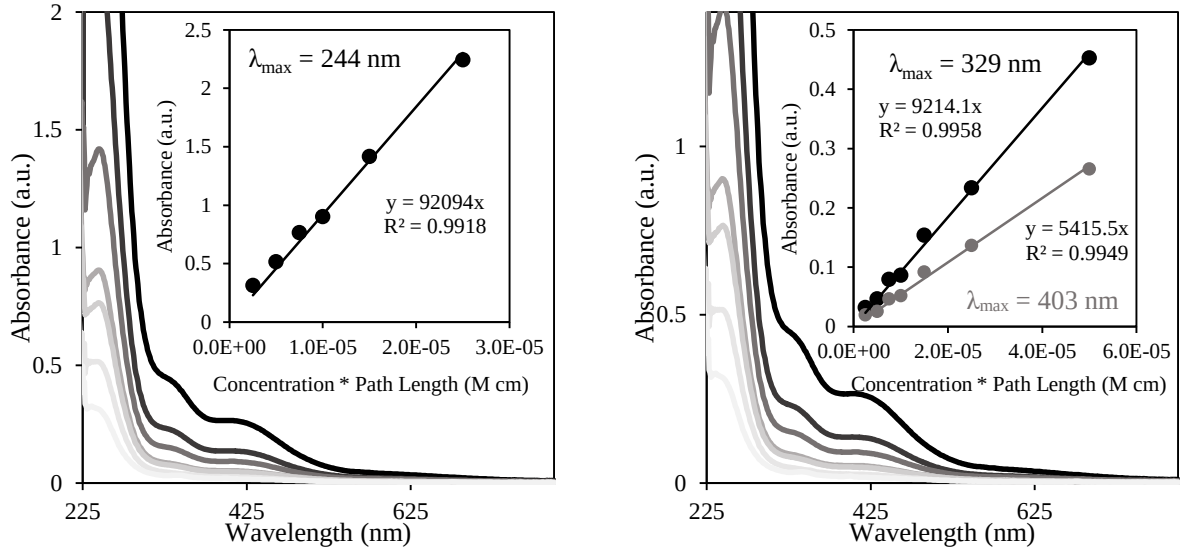


**Figure S45**. UV-Vis spectra of $[LFe_3F(PhPz)_3Fe(NO)][OTf]_2$ (**2-NO**) in $CH_2Cl_2$

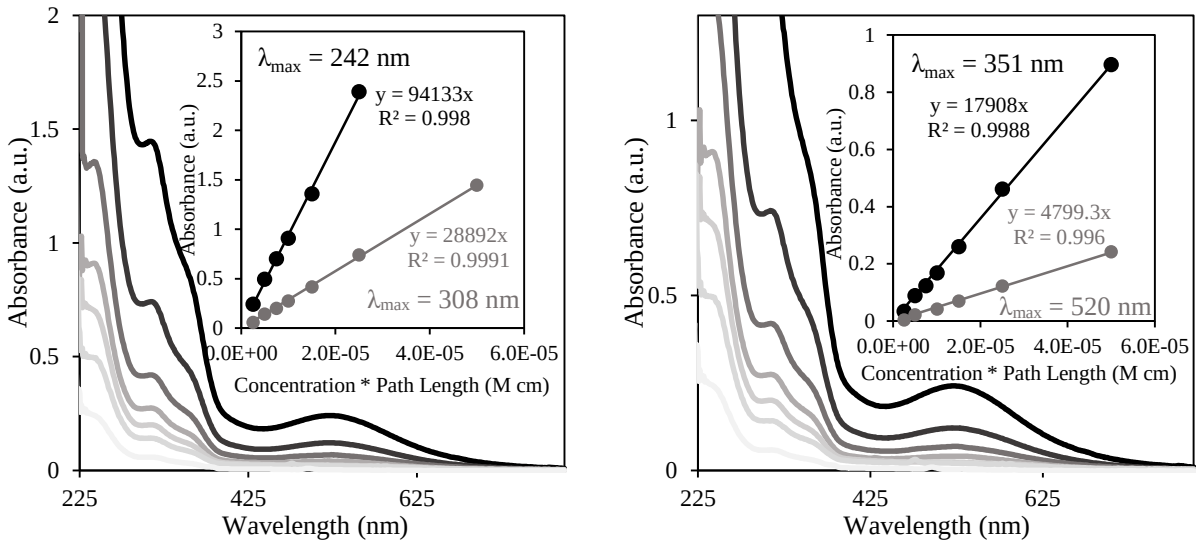


**Figure S46**. UV-Vis spectra of $[LFe_3F(PhPz)_3Fe(NO)][OTf]_3$ (**3-NO**) in $CH_2Cl_2$

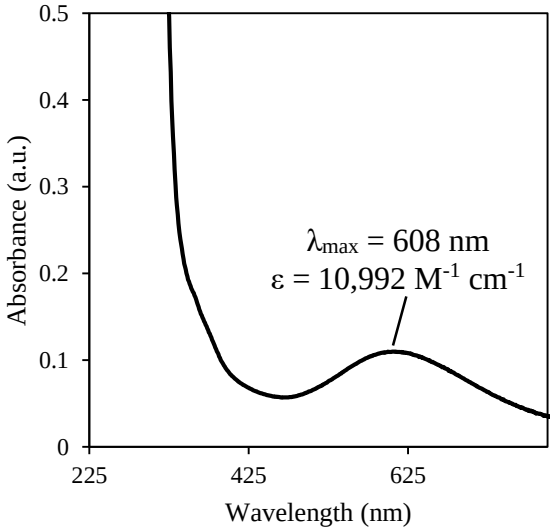


**Figure S47**. UV-Vis spectra of reaction product of $[LFe_3F(PhPz)_3Fe(NO)][OTf]_3$ with $[2,4\text{-}Br\text{-}C_6H_3)_3N][SbCl_6]$ in $CH_3CN$ (**4-NO**).

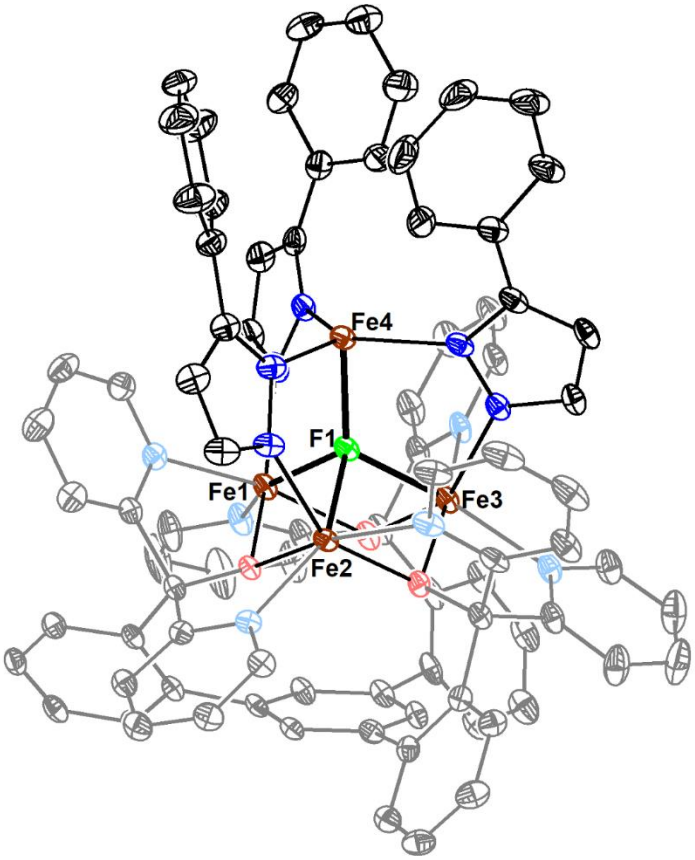


**Figure S48**. Crystal structure of [LFe$_3$F(PhPz)$_3$Fe][OTf] (**1**). Ellipsoids are shown at the 50% probability level. Hydrogen atoms, solvent molecules, and outersphere counterions omitted for clarity.

**Special refinement details for [LFe$_3$F(PhPz)$_3$Fe][OTf]**. The structure contains several co-crystallized solvent molecules, many of which are on special positions. The only complete solvent molecule in the asymmetric unit that could be refined was disordered over two positions refined as 34.1% (C14 through C102) and 65.9% (Cl2 through C101). The two remaining solvent molecules were also disordered over two positions, but on a symmetry element. One disordered dichloromethane was refined as a partially occupied carbon 25% (C103) with ~50% occupied chlorine groups (Cl6 and Cl7). The other disordered dichloromethane was refined as a half occupied molecule, disordered over a symmetry element.

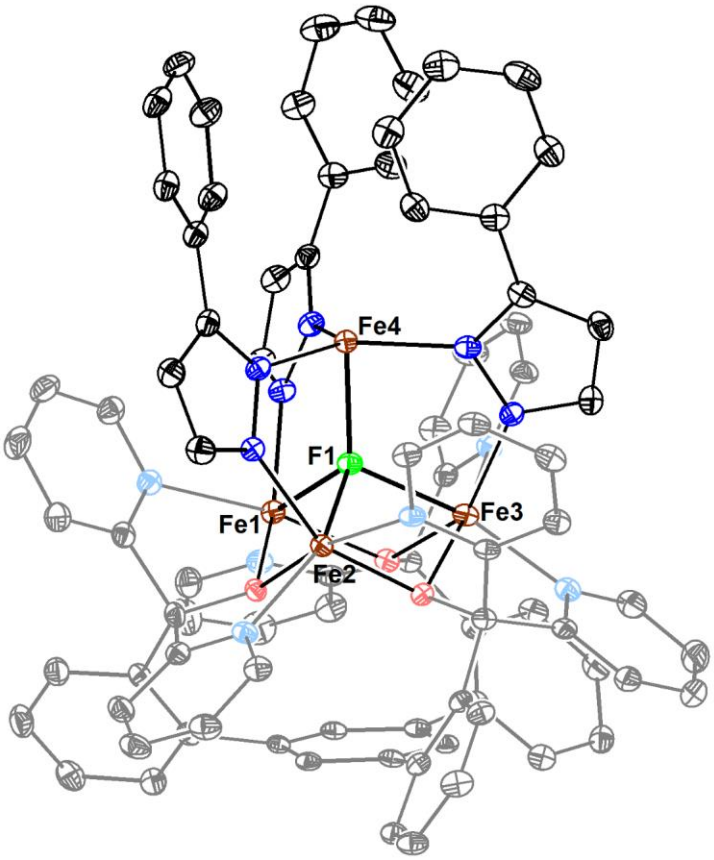


**Figure S49**. Crystal structure of $[LFe_3F(PhPz)_3Fe][OTf]_2$ (**2**). Ellipsoids are shown at the 50% probability level. Hydrogen atoms, solvent molecules, and outersphere counterions omitted for clarity.

**Special refinement details for $[LFe_3F(PhPz)_3Fe][OTf]_2$**. This structure contains two triflate counterions, one of which is positionally disordered over two positions with refined occupancies of 78.5% (S201 through C201) and 21.5% (S202 through C202). The structure also contains a co-crystallized dichloromethane (C0AA through Cl20), and two benzene molceules; one is complete (C101 through C106) the other (C107 through C109) is on a special position. Rigid bond restraints were used on the triflate counterions.

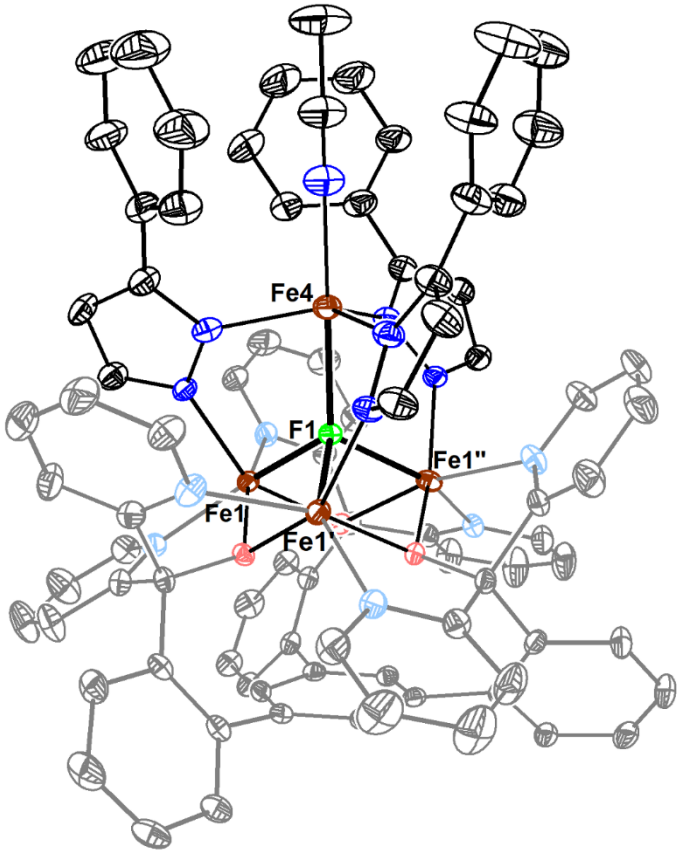


**Figure S50**. Crystal structure of $[LFe_3F(PhPz)_3Fe(CH_3CN)][OTf]_3$ (**3**). Ellipsoids are shown at the 50% probability level. Hydrogen atoms, solvent molecules, and outersphere counterions omitted for clarity.

**Special refinement details for $[LFe_3F(PhPz)_3Fe(CH_3CN)][OTf]_3$.** This structure contains the cluster on a $C_3$ rotation axis, and, therefore, the three irons in the tri-iron core (Fe1 through Fe1'') are indistinct. One triflate counterion is observed in the asymmetric unit along with four solvent molecules, only two of which could be modeled satisfactorily. A toluene molecule (C104 through C107) was disordered over a special position. There was another disordered toluene and acetonitrile that were disordered near special positions, based on residual electron density peaks; however, they could not be satisfactorily modeled. A solvent mask was used to account for the electron density of these molecules.

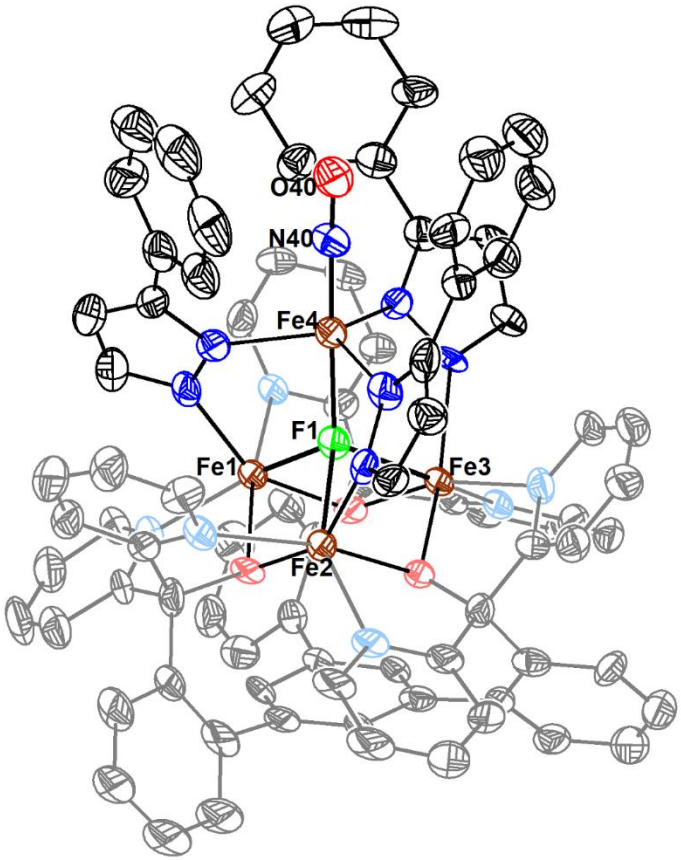


**Figure S51**. Crystal structure of [LFe$_3$F(PhPz)$_3$Fe(NO)][OTf] (**1-NO**). Ellipsoids are shown at the 50% probability level. Hydrogen atoms, solvent molecules, and outersphere counterions omitted for clarity.

**Special refinement details for [LFe$_3$F(PhPz)$_3$Fe(NO)][OTf]**. This structure contained numerous co-crystallized solvent molecules (eight dichloromethane molecules). One solvent molecule was disordered and modeled with occupancies of 69% (Cl111 through C105) and 31% (Cl8 through C104). Another dichloromethane contained a disordered chlorine atom that was modeled with occupancies of 63% (Cl15) and 37% (Cl14). The triflate counterion was positionally disordered, whereby the sulfur would point either towards or away from the cluster. It was refined as two molecules with occupancies of 61% (S200 through C200) and 39% (S201 through C201). The standard deviations of some atoms in the phenyl ring of the trinucleating ligand (C34 – C36) were restrained to be the same.

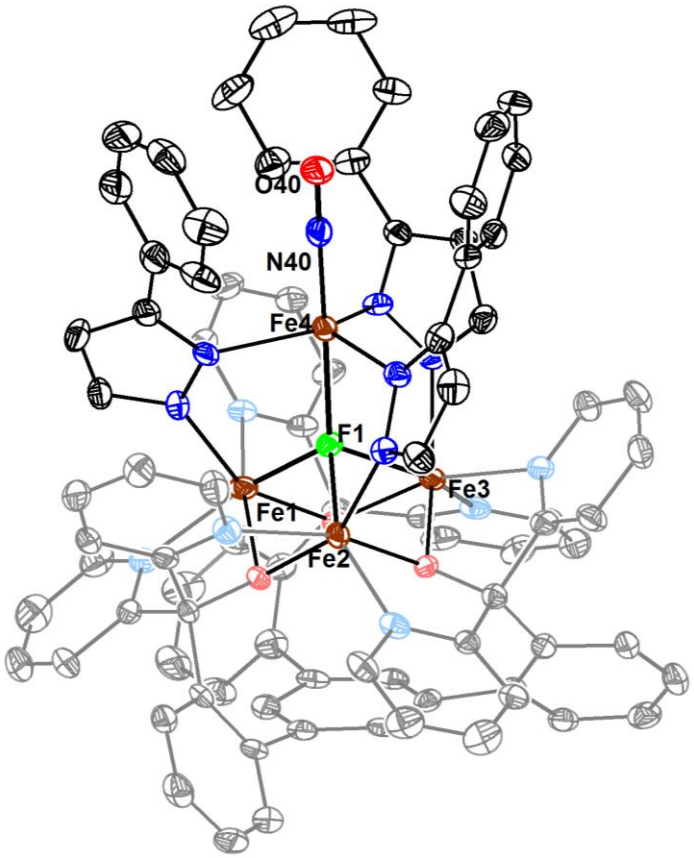


**Figure S52**. Crystal structure of $[LFe_3F(PhPz)_3Fe(NO)][OTf]_2$ (**2-NO**). Ellipsoids are shown at the 50% probability level. Hydrogen atoms, solvent molecules, and outersphere counterions omitted for clarity.

**Special refinement details for $[LFe_3F(PhPz)_3Fe(NO)][OTf]_2$**. The structure contains two triflate counterions. One counterion is disordered over two positions with occupancies of 79.3% (S202 through C202) and 20.7% (S201 through C201). Three of the seven co-crystallized dichloromethane molecules are disordered over two positions. The first has occupancies of 59% (Cl11 through C105) and 41% (C103 through C108).

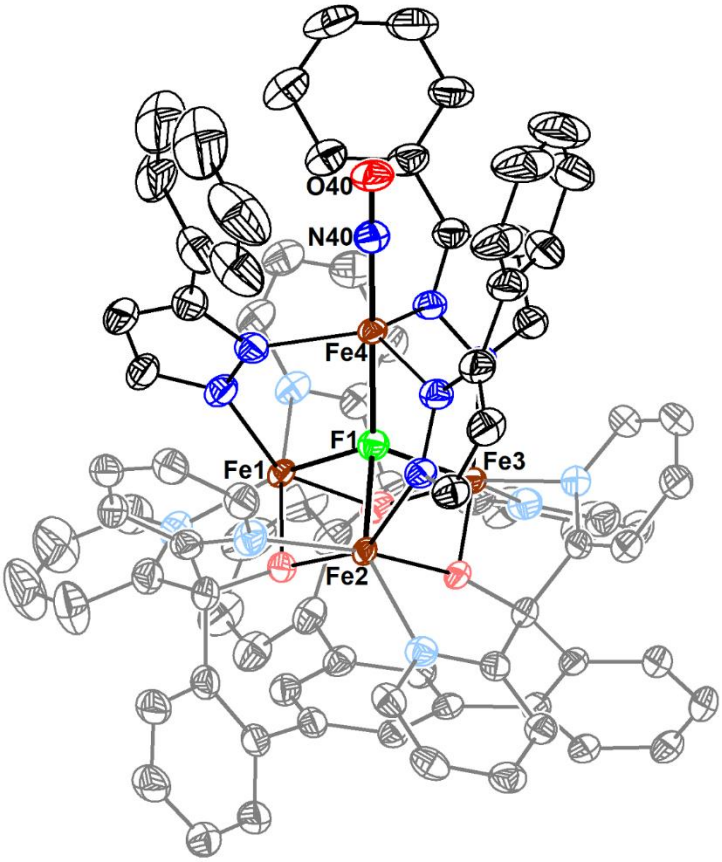


**Figure S53**. Crystal structure of $[LFe_3F(PhPz)_3Fe(NO)][OTf]_3$ (**3-NO**). Ellipsoids are shown at the 50% probability level. Hydrogen atoms, solvent molecules, and outersphere counterions omitted for clarity.

**Special refinement details for $[LFe_3F(PhPz)_3Fe(NO)][OTf]_3$**. There are two molecules in the asymmetric unit of the crystal structure. One of the clusters (Fe0A through C199) has a disordered phenyl pyrazolate ligand. Because of this disorder, the bond lengths and angles were not considered with in this molecule and only the other cluster, for which there was no evidence of disorder, (Fe1 through C99) was used for reporting bond metrics. All but two triflate counterions were disordered. Three triflates were positionally disordered; the first two had occupancies of 78% (S303 through C303 and S304 through C304) and 22% (S302 through C302 and S305 through C305). The third triflate had occupancies of 76% (S306 through C306) and 24% (S307 thgouh C307). The two remaining triflates were disordered as a pair. They could be modeled as being adjacent to one another with occupancies of 51% (S308 through C308) and 62% (S130 through C130). This would be disordered with two triflates, one occupying the same space as the first pair with an occupancy of 37% (S309 through C309), and the other, itself disordered, next to a symmetry element with an occupancy of 50%. There were seven dichloromethane solvent molecules modeled in the structure. Two had positionally disordered chlorine atoms with occupancies of 78% (Cl9) and 22% (Cl16), and 51% (Cl5) and 49% (Cl6). Another dichloromethane was only partially occupied (taking up the same space as the disordered pair of triflates, as discussed above); it had an occupancy of 36% (Cl10 through C205).

| | Complex | | | | | |
|---|---|---|---|---|---|---|
| **Bond Distance (Å)** | **1** | **2** | **3** | **1-NO** | **2-NO** | **3-NO** |
| Fe1–F1 | 2.167(1) | 2.024(1) | 2.132(2) | 2.129(7) | 2.030(4) | 2.207(3) |
| Fe2–F1 | 2.154(1) | 2.204(1) | – | 2.205(6) | 2.237(4) | 2.080(3) |
| Fe3–F1 | 2.174(1) | 2.216(1) | – | 2.169(5) | 2.101(4) | 2.091(3) |
| Fe4–F1 | 1.997(1) | 2.011(1) | 2.172(4) | 2.065(7) | 2.093(4) | 2.155(3) |
| Fe1–N13 | 2.170(2) | 2.076(2) | 2.061(3) | 2.118(10) | 2.076(5) | 2.057(4) |
| Fe2–N23 | 2.187(2) | 2.125(2) | – | 2.122(8) | 2.102(5) | 2.046(4) |
| Fe3–N33 | 2.157(2) | 2.108(2) | – | 2.116(11) | 2.083(6) | 2.025(4) |
| Fe4–N14 | 2.034(2) | 2.063(2) | | 2.049(10) | 2.064(6) | 2.020(4) |
| Fe4–N24 | 2.056(2) | 2.056(2) | – | 2.060(9) | 2.057(6) | 2.049(4) |
| Fe4–N34 | 2.046(2) | 2.044(2) | – | 2.044(10) | 2.064(5) | 2.025(4) |
| N13–N14 | 1.390(2) | 1.386(3) | 1.387(5) | 1.401(15) | 1.389(7) | 1.369(6) |
| N23–N24 | 1.383(2) | 1.389(3) | – | 1.398(13) | 1.380(8) | 1.371(6) |
| N33–N34 | 1.387(2) | 1.388(3) | – | 1.384(13) | 1.379(8) | 1.389(5) |
| Fe4–N40 | – | – | 2.112(8) | 1.757(10) | 1.773(6) | 1.754(4) |
| N40–O40 | – | – | – | 1.163(13) | 1.147(7) | 1.133(6) |
| **Bond Angles (º)** | | | | | | |
| N14–Fe4–N24 | 119.24(7) | 119.34(8) | 117.323 | 118.5(4) | 114.6(2) | 119.99(2) |
| N24–Fe4–N34 | 117.34(7) | 120.91(8) | – | 117.1(4) | 119.8(2) | 116.37(2) |
| N34–Fe4–N14 | 123.35(7) | 119.26(8) | – | 119.1(4) | 119.6(2) | 114.83(2) |
| Fe4–N40–O40 | – | – | – | 175.7(9) | 177.0(6) | 179.2(4) |
| **Torsion Angles (º)** | | | | | | |
| Fe1–N13–N14–Fe4 | 3.640 | 3.40 | 27.095 | 23.02 | 29.86 | 23.320 |
| Fe2–N23–N24–Fe4 | 1.317 | 4.02 | - | 31.89 | 30.26 | 23.035 |
| Fe3–N33–N34–Fe4 | 4.968 | 2.14 | - | 30.32 | 22.64 | 25.985 |
| **Centroid Distances (Å)** | | | | | | |
| Fe1\|Fe2\|Fe3–N14\|N24\|N34 | 3.090 | 2.972 | 2.832 | 2.889 | 2.856 | 2.828 |
| Fe1\|Fe2\|Fe3–O11\|O21\|O31 | 0.974 | 0.945 | 1.008 | 0.959 | 0.987 | 0.926 |
| Fe1\|Fe2\|Fe3–F1 | 1.093 | 1.051 | 0.975 | 1.100 | 1.063 | 1.029 |
| N14\|N24\|N34–Fe4 | 0.053 | 0.084 | 0.344 | 0.276 | 0.296 | 0.353 |

**Table S1**. Selected bond angles and distances for complexes **1-3**, **1-NO** – **3-NO**.

| | **1** | **2** | **3** |
|---|---|---|---|
| CCDC Number | 1554599 | 1554601 | 1554596 |
| Empirical formula | $C_{86.75}H_{62}Cl_4F_4Fe_4N_{12}O_6S$ | $C_{96}H_{71}Cl_2F_7Fe_4N_{12}O_9S_2$ | $C_{101.5}H_{75}F_{10}Fe_4N_{14}O_{12}S_3$ |
| Formula weight | 1837.80 | 2028.06 | 2235.21 |
| Radiation | MoKα (λ = 0.71073) | MoKα (λ = 0.71073) | MoKα (λ = 0.71073) |
| a (Å) | 12.4213(18) | 40.6924(19) | 16.1006(6) |
| b (Å) | 16.108(2) | 17.6138(8) | 16.1006(6) |
| c (Å) | 20.502(3) | 25.6670(13) | 67.515(3) |
| α (°) | 78.323(6) | 90 | 90 |
| β (°) | 78.274(7) | 114.015(2) | 90 |
| γ (°) | 85.537(6) | 90 | 120 |
| V (Å$^3$) | 3930.6(10) | 16804.3(14) | 15157.0(13) |
| Z | 2 | 8 | 6 |
| Cryst. syst. | triclinic | monoclinic | trigonal |
| Space group | P-1 | C2/c | R-3 |
| $\rho_{calc}$g (cm$^3$) | 1.553 | 1.603 | 1.469 |
| 2 Θ range (°) | 2.584 to 61.034 | 4.626 to 55.754 | 5.060 to 61.146 |
| μ (mm$^{-1}$) | 0.960 | 0.877 | 0.712 |
| GOF | 0.998 | 1.026 | 1.051 |
| R1, wR2 (I>2σ (I)) | 0.0400, 0.1003 | 0.0458, 0.0959 | 0.0835, 0.2216 |

| | **1-NO** | **2-NO** | **3-NO** |
|---|---|---|---|
| CCDC Number | 1554600 | 1554598 | 1554597 |
| Empirical formula | $C_{93}H_{76}Cl_{16}F_4Fe_4N_{13}O_7S$ | $C_{93}H_{74}Cl_{14}F_7Fe_4N_{13}O_{10}S_2$ | $C_{89.92}H_{64.86}Cl_{5.85}F_{10}Fe_4N_{13}O_{13}S_3$ |
| Formula weight | 2386.32 | 2450.16 | 2252.38 |
| Radiation | CuKα (λ = 1.54178) | MoKα (λ = 0.71073) | CuKα (λ = 1.54178) |
| a (Å) | 18.7000(7) | 20.1692(15) | 17.8680(9) |
| b (Å) | 16.8237(7) | 17.4343(13) | 20.4024(11) |
| c (Å) | 32.4277(11) | 28.440(2) | 26.3282(15) |
| α (°) | 90 | 90 | 78.386(4) |
| β (°) | 103.821(2) | 99.091(2) | 72.564(3) |
| γ (°) | 90 | 90 | 82.836(3) |
| V (Å$^3$) | 9906.5(7) | 9874.8(13) | 8948.2(9) |
| Z | 4 | 4 | 4 |
| Cryst. syst. | monoclinic | monoclinic | triclinic |
| Space group | $P2_1/n$ | $P2_1/n$ | P-1 |
| $\rho_{calc}$g (cm$^3$) | 1.600 | 1.648 | 1.672 |
| 2 Θ range (°) | 5.004 to 130.168 | 4.464 to 51.356 | 9.042 to 179.202 |
| μ (mm$^{-1}$) | 9.351 | 1.076 | 8.167 |
| GOF | 1.052 | 1.060 | 1.033 |
| R1, wR2 (I>2σ (I)) | 0.1232, 0.2937 | 0.0944, 0.2594 | 0.0786, 0.2045 |

**Table S2**. Crystal and refinement data for complexes **1** – **3** and **1-NO** – **3-NO**.

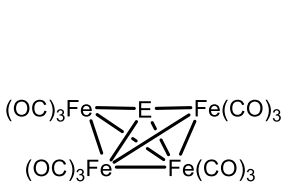


**$[Fe_4E(CO)_{12}]^{n-}$**

E = C, N

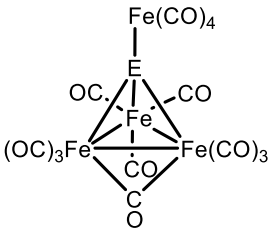


**$[Fe_4E(CO)_{14}]^{n-}$**

E = P, As, Ge*

*-$\mu_2$-CO +$\mu_3$-CO

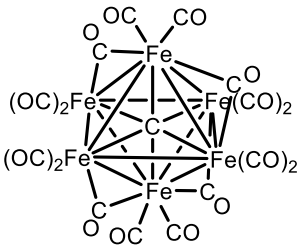


**$[Fe_6C(CO)_{16}]^{2-}$**

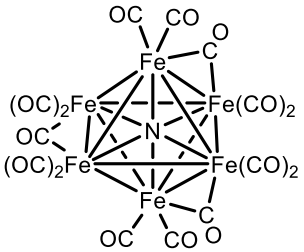


**$[Fe_6N(CO)_{15}]^{3-}$**

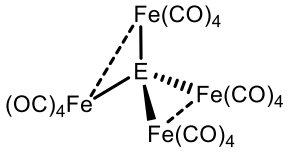


**$[Fe_4E(CO)_{16}]^{n-}$**

E =Si, Zn, Ge, Pd, Cd, In, Sn, Sb, Te, Pt, Au, Hg, Pb, Bi

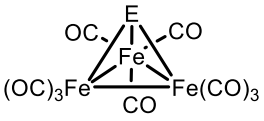


**$[Fe_3E(CO)_9]^{n-}$**

E = O, S, Se, Te, Bi*

*+$\mu_3$-CO

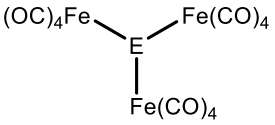


**$[Fe_3E(CO)_{12}]^{n-}$**

E = Se, In, Sn, Te, Tl, Pb

**Table S3.** Reported C–O Stretching Frequencies and Redox Potentials for Iron Carbonyl Clusters Bearing Various Interstitial Ligands.

| Compound | E (V vs SCE) | $\nu_{CO}$ ($cm^{-1}$) | Ref |
|---|---|---|---|
| $[Fe_4C(CO)_{12}]^{2-}$ | -1.75 *(2-/3-)*[a] | 1969, 1945 (3-: 1874)[b] | 3 |
| $[Fe_4N(CO)_{12}]^{-}$ | 0.2 *(0/-)*, -1.23 *(-/2-)*, -1.6 *(2-/3-)* [a] | 2018, 1989 (2-: 1940)[b] | 3b, 3c, 4 |
| $[Fe_4P(CO)_{14}]^{-}$ | | 2040, 2020, 1875 | 5 |
| $[Fe_4As(CO)_{14}]^{-}$ | | 2056, 2028, 2012, 2000, 1965, 1939, 1794 | 6 |
| $[Fe_4Ge(CO)_{14}]^{2-}$ | | 1998, 1963, 1917, 1720 | 7 |
| $[Fe_6C(CO)_{16}]^{2-}$ | | 1964, 1957, 1930, 1775 | 8 |
| $[Fe_6N(CO)_{15}]^{3-}$ | -0.39 *(2-/3-)*, -0.19 *(-/2-)*, +0.2 *(0/-)* [a] | 1956, 1914, 1844, 1740 | 9 |
| $[Fe_4Si(CO)_{16}]$ | | 2076, 2050, 2030, 2013 | 10 |
| $[Fe_4Zn(CO)_{16}]^{2-}$ | | 1999, 1978, 1936, 1750 | 11 |
| $[Fe_4Ge(CO)_{16}]$ | | 2078, 2050, 2030, 2015 | 12 |
| $[Fe_4Pd(CO)_{16}]^{2-}$ | | 2035, 1980, 1970, 1960, 1940, 1910, 1850 | 13 |
| $[Fe_4Cd(CO)_{16}]^{2-}$ | | 2000, 1985, 1935, 1927, 1755 | 11 |
| $[Fe_4In(CO)_{16}]^{-}$ | | 2041, 2010, 1970, 1962, 1951 | 14 |
| $[Fe_4Sn(CO)_{16}]^{2-}$ | 0.44 *(0/2-)* [a], 0.98 | 2050, 2003, 1990, 1975, 1899, 1793 | 7 |

| | | | |
|---|---|---|---|
| $[Fe_4Sb(CO)_{16}]^-$ | | 2086, 2042, 2020, 1922 | 15 |
| $[Fe_4Te(CO)_{16}]^{2-}$ | | 2006, 1936, 1921 | 16 |
| $[Fe_4Pt(CO)_{16}]^{2-}$ | 0.01 *(-/2-)* [a] | 2020, 1985, 1970, 1960, 1935, 1925, 1830 | 13 |
| $[Fe_4Au(CO)_{16}]^-$ | -0.73 *(-/2-)*, -0.93 *(2-/3-)* [a] | 2015, 1990, 1957 (2-: 1948, 1945, 1770; 3-: 1979, 1931, 1766)[b] | 17 |
| $[Fe_4Hg(CO)_{16}]^{2-}$ | | 2020, 1984, 1930, 1740 | 11 |
| $[Fe_4Pb(CO)_{16}]^{2-}$ | -0.64 *(4-/2-)*, 0.26 *(0/-2)* [a] | 2042, 1999, 1975, 1900, 1777 | 7, 18 |
| $[Fe_4Bi(CO)_{16}]^{3-}$ | | 1962, 1906, 1867 | 19 |
| $[Fe_3O(CO)_9]^{2-}$ | | 2000, 1928, 1899, 1869 | 20 |
| $[Fe_3S(CO)_9]^{2-}$ | | 1997, 1927, 1901, 1870 | 20 |
| $[Fe_3Se(CO)_9]^{2-}$ | | 1995, 1926, 1897, 1870 | 21 |
| $[Fe_3Te(CO)_9]^{2-}$ | | 1992, 1924, 1895, 1868 | 21 |
| $[Fe_3Bi(CO)_{10}]^-$ | | 2035, 1983, 1946 | 19 |
| $[Fe_3Se(CO)_{12}]^{2-}$ | | 2040, 1996, 1932, 1897 | 21 |
| $[Fe_3In(CO)_{12}]^{3-}$ | | 1935, 1849 | 22 |
| $[Fe_3Sn(CO)_{12}]^{2-}$ | | 2021, 2002, 1977, 1904 | 23 |
| $[Fe_3Te(CO)_{12}]^{2-}$ | | 2020, 1985, 1926, 1900 | 21 |
| $[Fe_3Tl(CO)_{12}]^{3-}$ | | 1984, 1925, 1850 | 24 |
| $[Fe_3Pb(CO)_{12}]^{2-}$ | | 1973, 1895 | 23 |

[a] Reported cluster charge state assignments are given in parentheses next to the redox potential
[b] Reported CO stretching frequencies for clusters of different charge state are given in parentheses

## References


1. (a) de Ruiter, G.; Thompson, N. B.; Lionetti, D.; Agapie, T. *J. Am. Chem. Soc.* **2015,** *137*, 14094-14106; (b) de Ruiter, G.; Thompson, N. B.; Takase, M. K.; Agapie, T. *J. Am. Chem. Soc.* **2016,** *138*, 1486-1489; (c) Herbert, D. E.; Lionetti, D.; Rittle, J.; Agapie, T. *J. Am. Chem. Soc.* **2013,** *135*, 19075-19078.
2. (a) Herold, S.; Lippard, S. J. *Inorg. Chem.* **1997,** *36*, 50-58; (b) Singh, A. K.; Jacob, W.; Boudalis, A. K.; Tuchagues, J.-P.; Mukherjee, R. *Eur. J. Inorg. Chem.* **2008,** *2008*, 2820-2829; (c) Sutradhar, M.; Carrella, L. M.; Rentschler, E. *Eur. J. Inorg. Chem.* **2012,** *2012*, 4273-4278; (d) Schünemann, V.; Hauke, P. Mössbauer Spectroscopy. In *Applications of Physical Methods to Inorganic and Bioinorganic Chemistry*, Scott, R. A.; Lukehart, C. M., Eds. John Wiley & Sons: West Sussex, England, 2007; pp 243-269.
3. (a) Boehme, R. F.; Coppens, P. *Acta Crystallographica Section B* **1981,** *37*, 1914-1916; (b) Nguyen, A. D.; Rail, M. D.; Shanmugam, M.; Fettinger, J. C.; Berben, L. A. *Inorg. Chem.* **2013,** *52*, 12847-12854; (c) Taheri, A.; Berben, L. A. *Inorg. Chem.* **2016,** *55*, 378-385.
4. (a) Fjare, D. E.; Gladfelter, W. L. *Inorg. Chem.* **1981,** *20*, 3533-9; (b) Taheri, A.; Thompson, E. J.; Fettinger, J. C.; Berben, L. A. *ACS Catalysis* **2015,** *5*, 7140-7151.
5. Gourdon, A.; Jeannin, Y. *J. Organomet. Chem.* **1986,** *304*, C1-C3.
6. Schipper, D. E.; Young, B. E.; Whitmire, K. H. *Organometallics* **2016,** *35*, 471-483.
7. Whitmire, K. H.; Lagrone, C. B.; Churchill, M. R.; Fettinger, J. C.; Robinson, B. H. *Inorg. Chem.* **1987,** *26*, 3491-3499.
8. (a) Churchill, M. R.; Wormald, J. *J. Chem. Soc., Dalton Trans.* **1974**, 2410-2415; (b) Churchill, M. R.; Wormald, J.; Knight, J.; Mays, M. J. *J. Am. Chem. Soc.* **1971,** *93*, 3073-3074; (c) Kuppuswamy, S.; Wofford, J. D.; Joseph, C.; Xie, Z.-L.; Ali, A. K.; Lynch, V. M.; Lindahl, P. A.; Rose, M. J. *Inorg. Chem.* **2017,** *56*, 5998-6012.
9. Pergola, R. D.; Bandini, C.; Demartin, F.; Diana, E.; Garlaschelli, L.; Stanghellini, P. L.; Zanello, P. *J. Chem. Soc., Dalton Trans.* **1996**, 747-754.
10. Anema, S. G.; Barris, G. C.; Mackay, K. M.; Nicholson, B. K. *J. Organomet. Chem.* **1988,** *350*, 207-215.
11. Albano, V. G.; Monari, M.; Demartin, F.; Macchi, P.; Femoni, C.; Iapalucci, M. C.; Longoni, G. *Solid State Sciences* **1999,** *1*, 597-606.
12. Batsanov, A. S.; Rybin, L. V.; Rybinskaya, M. I.; Struchkov, Y. T.; Salimgareeva, I. M.; Bogatova, N. G. *J. Organomet. Chem.* **1983,** *249*, 319-326.
13. Longoni, G.; Manassero, M.; Sansoni, M. *J. Am. Chem. Soc.* **1980,** *102*, 3242-3244.
14. Lin, C. C.; Kong, G.; Cho, H.; Whittlesey, B. R. *Inorg. Chem.* **1993,** *32*, 2705-2710.
15. Luo, S.; Whitmire, K. H. *J. Organomet. Chem.* **1989,** *376*, 297-310.
16. Roof, L. C.; Smith, D. M.; Drake, G. W.; Pennington, W. T.; Kolis, J. W. *Inorg. Chem.* **1995,** *34*, 337-345.
17. Albano, V. G.; Aureli, R.; Lapalucci, M. C.; Laschi, F.; Longoni, G.; Monari, M.; Zanello, P. *J. Chem. Soc., Chem. Commun.* **1993**, 1501-1502.
18. Lagrone, C. B.; Whitmire, K. H.; Churchill, M. R.; Fettinger, J. C. *Inorg. Chem.* **1986,** *25*, 2080-2085.
19. Whitmire, K. H.; Lagrone, C. B.; Churchill, M. R.; Fettinger, J. C.; Biondi, L. V. *Inorg. Chem.* **1984,** *23*, 4227-4232.

20. Schauer, C. K.; Harris, S.; Sabat, M.; Voss, E. J.; Shriver, D. F. *Inorg. Chem.* **1995,** *34,* 5017-5028.
21. Bachman, R. E.; Whitmire, K. H. *Inorg. Chem.* **1994,** *33,* 2527-2533.
22. Albano, V. G.; Cané, M.; Iapalucci, M. C.; Longo, G. *J. Organomet. Chem.* **1991,** *407,* C9-C12.
23. Cassidy, J. M.; Whitmire, K. H. *Inorg. Chem.* **1989,** *28,* 2494-2496.
24. van Hal, J. W.; Alemany, L. B.; Whitmire, K. H. *Inorg. Chem.* **1997,** *36,* 3152-3159.